BAJECE

e-mail: editor@bajece.com

Balkan Journal of Electrical & Computer Engineering

An International Peer Reviewed, Refereed, Indexed and Open Access Journal

www.bajece.com

Vol : 2
No : 1
Year : 2014
ISSN : 2147-284X

Sponsored by the

- Kirklareli University,
- Klaipeda University
- Inonu University
- Istanbul Technical University
- City University London
- Sriwijaya University

This journal is accredited by the Kirklareli University subsidy purposes. It is abstracted and indexed in Copernicus, Index Google Scholarship, the PSCR, DOAJ, Research Bible, Indian Open Access Journals (OAJ), Institutional Repositories (IR), Journal TOCs, J-Gate (Informatics India), Ulrich's, ResearchGate, International Society of Universal Research in Sciences, DRJI, EyeSource.

Aim & Scope

The journal publishes original papers in the extensive field of Electrical-Electronics and Computer engineering. It accepts contributions which are fundamental for the development of electrical engineering, computer engineering and its applications, including overlaps to physics. Manuscripts on both theoretical and experimental work are welcome. Review articles and letters to the editors are also included.
Application areas include (but are not limited to): Electrical & Electronics Engineering, Computer Engineering, Software Engineering, Biomedical Engineering, Electrical Power Engineering, Control Engineering, Signal and Image Processing, Communications & Networking, Sensors, Actuators, Remote Sensing, Consumer Electronics, Fiber-Optics, Radar and Sonar Systems, Artificial Intelligence and its applications, Expert Systems, Medical Imaging, Biomedical Analysis and its applications, Computer Vision, Pattern Recognition, Robotics, Industrial Automation.

BAJECE

Balkan Journal of Electrical & Computer Engineering

An International Peer Reviewed Refereed indexed and Open Access Journal

ISSN: 2147- 284X
Vol: 2
No : 1
Year: March 2014

CONTENTS

BALKAN JOURNAL OF ELECTRICAL & COMPUTER ENGINEERING
(An International Peer Reviewed, Refereed, indexed and Open Access Journal**)**

Contact
https://www.bajece.com

e-mail: editor@bajece.com
bajece@bajece.com

Phone: +90 288 214 05 14
Fax: +90 288 214 05 16
Kirklareli University, Department of Electrical & Electronics Engineering, 39060, Kirklareli-Turkey.

The Influence of Radiation on the Solar Cell Efficiency

H.Šamić and S.Makham

***Abstract*—The use of a solar cell in space requires the knowledge of its behavior under high-energy partial radiation. This radiation in space produces defects in semiconductor that cause a reduction in solar cell power output. In this paper we present the method for predicting the behavior of a solar cell for satellite applications. Modeling has been performed for several types of GaAs and GaInP single cells and results are compared with experimental data obtained for electron and proton irradiations.**

Index Terms—**Solar cells, GaAs, GaInP, degradation, radiation defects**

INTRODUCTION

As worldwide energy demand increases, conventional energy resources will be exhausted in the not-too-distant future. Therefore, the solar cell is the major candidate for obtaining energy from sun, since it can provide nearly permanent power at low operating cost and almost free of pollution.

Solar cells at present furnish the most important long-duration power supply for satellites and space vehicles and have also been successfully employed in terrestrial applications.

The evaluation of solar cell degradation in space is very important now that multijonction (MJ) cells are used to fill the need for increasing power in satellites. Materials, mostly III-V semiconductors and many of their ternary alloys are used to produce multijonction cells. The study of solar cell degradation has been long standing for Si but is new for GaInP and other alloys. It is well known that the diffusion length[(1)] in Si and GaAs and the minority lifetime will increase as the temperature increases. The increase in minority-carrier diffusion length causes an increase in short-circuit current Jsc. However, open-circuit voltage V_{oc} will rapidly decrease because of the exponential dependence of the saturation current on temperature. For satellite and deep space missions, the knowledge of solar cells behavior under electron and proton irradiations present in space, and assessing the expected useful life of the space solar cell power plant is very important.

The high-energy particles introduce non-radiative recombination centers as result of the displacements of atoms induced by their collisions with these particles. The recombination centers [(2)] reduce the minority carrier lifetime and the collection of the electrons and holes generated by light absorption. This reduction causes the decrease of the short-circuit current J_{sc} , open-circuit voltage V_{oc} and finally maximum power P_m.

In this paper the degradation of GaAs and GaInP single solar cells, from the characteristic of the defects introduced by electron and proton irradiation is reported.

RADIATION EFFECTS

The way to evaluate the degradation induced by given fluence φ of irradiation consists of computing the I-V characteristics of the cell using values of the minority lifetime τ in the emitter and base taking account the concentrations N of the non-radiative centers introduced by irradiation:

$$N = k\varphi \tag{1}$$

where k is introduction rate of the defects that act as recombination centers and

$$\frac{1}{\tau} = \frac{1}{\tau_0} + kv_{th}\varphi\sigma \tag{2}$$

τ_o is the value of the lifetime prior to irradiation called BOL (for beginning of life), v_{th} the thermal velocity of the carriers and σ the cross-section for minority carrier capture on the irradiation induced recombination centers. The photocurrent will decrease with decreasing diffusion lengths of carriers L. Since diffusion length is equal to $(D_\tau)^{1/2}$ it is important to determinate degradation parameters k and σ . The determination of the k and σ is complicated because several different defects [(3)] are usually created by irradiation. Until recently was used the concept of relative damage coefficient (RDC) or equivalent fluence [(4-5)]. In order to reduce the number of irradiations tests, a RDC coefficient relates the fluence φ at a given energy E which produce the same degradation as fluence φ_0 at standard energy E_o. According this concept the degradations follows the empirical law:

H. Šamić is with the Faculty of Electrical Engineering, University of Sarajevo, Sarajevo, Bosnia and Herzegovina (e-mail: hsamic@etf.unsa.ba).

S. Makham is with GESEC R&D, Thomery, France, (e-mail: samiramakham@yahoo.fr).

$$\frac{P_m}{P_{m0}} = 1 - C\ln(1+\frac{\varphi}{\varphi_0}) \quad (3)$$

where $\frac{P_m}{P_{m0}}$ is normalized maximum power after irradiation, C and φ_0 are empirical constants, whose values are different for electron and proton irradiations and for each parameter (V_{oc}, I_{sc} and P_m) they are specific to given cell and given type of irradiation.

In this paper we used a new approach [6] based on equivalence between two particles, electron and proton. Systematic studies, combining measurements electroluminescence, time resolved photoluminescence (TRLP) and deep level transient spectroscopy (DLTS) performed on GaAs and GaInP junctions [7-8] gave as the concentrations and the introduction rates of the native and irradiation induced defects in each material.

We proposed that the degradation of one cell under the irradiation fluence φ_i and energy Ei is the same as the degradation under the irradiation fluence φ_j and energy E_j, if the nature and concentrations of non-radiative centers produced by irradiations is the same, that means $N_i = N_j$. This concept is valid [3] in the cases of GaAs and GaInP but not for Si cells, because the defects created by electrons and protons are the same, since they result directly from the transmission of energy to the primary knock-on atom and the displaced atoms are separated by an average large distance. Also, the natures and concentrations of the defects introduced by irradiation in these two materials do not depend on the nature and concentration of the impurities and native defects in materials. That means, if the introduction rates k and capture cross-section σ of recombination centers in Gas are known for 1MeV electrons, we could determine these parameters for the protons different energies.
Using SRIM program and already known values of introduction rate *k*=0,1cm^{-1} for GaAs cell under 1 MeV electrons and energy loss per particle En_l =1.4x10^2 eVcm^{-1} we determined [9] the introduction rates k for recombination centers introduced by protons different energies. (Fig.1)

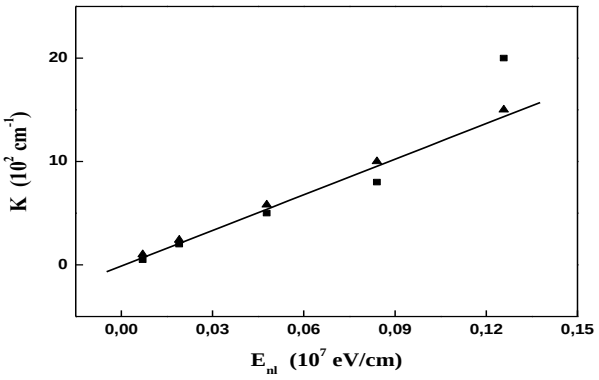

Fig. 1. Variation of the introduction rate of the recombination centers in the base (■) and in the emitter (▲) versus energy loss per proton for GaAs cell.

The same as for GaAs cell, we applied principle electron - proton equivalence on the GaInP cell using date for 1MeV electron published by NRL[10] for Enl (1MeV) =3,17x10^{-5} MeVcm^2/g and k ≈ 0.17 cm^{-1} (7) to obtained introduction rate of recombination centers introduced by protons irradiation (Fig.2)

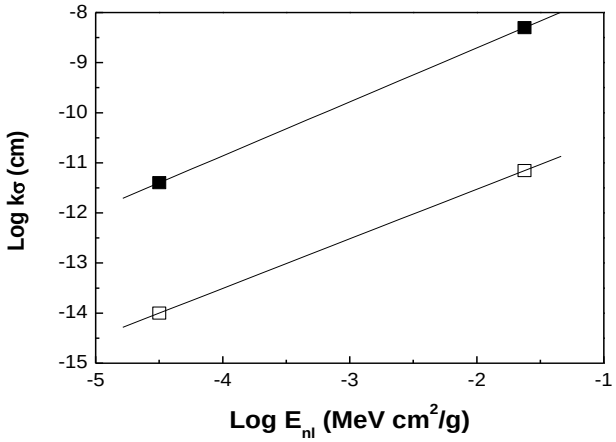

Fig.2.Variation of the degradation parameters $k_n\sigma_n$ (■) and $k_p\sigma_p$ (□) versus energy loss per electrons and protons in atomic collisions for GaInP cell NRL.

Once the k σ values are known for each material, it is possible to deduce the variations of V_{oc}, J_{sc} and P_m versus the fluence of irradiation.

MODELLIZATION OF THE DEGRADATION

Our modeling procedure consists to use the classical equations given in textbooks [11], describing the I-V characteristic of a solar cell under illumination. The short circuit current Jsc is sum of the three components, the photocurrents J generated in the emitter (e), the base (b) and the space charge region (z):

$$J_{SC} = J_e + J_z + J_b = J_{SC}(d_w, d_e, w, d_b, \phi, \alpha, \beta, S_e) \quad (4)$$

Where d_b, d_e and d_w are the thickness of the base, emitter and window, respectively, w is thickness of the depletion region, α and β are absorption coefficients of the cell material and of the window and S_e is recombination velocity at the emitter interface. The open circuit voltage V_{oc} is given by the following expression:

$$V_{oc} = \frac{2k_bT}{q}\ln\left(\frac{J_{sc}}{J_R}\right) \quad (5)$$

The recombination current $J_R(w,\varphi)$ contains three terms:

$$J_R(w,\varphi) = \frac{\pi}{2}n_i k_b T w\sqrt{\frac{1}{\tau_e\tau_b V_d^2}} + qn_i w\left(\frac{1}{\tau_{ob}^*} + \frac{1}{\tau_{oe}^*} + \frac{1}{\tau_b^*} + \frac{1}{\tau_e^*}\right) \quad (6)$$

where $\tau^*_{oe,b}$ and $\tau^*_{e,b}$ are the effective lifetimes of minority

carriers in the emitter and base before and after irradiation, respectively.

The maximum power Pm is obtained through the derivative of the product *VJ* relative to *V*. The photocurrent *J* is difference between the short circuit current and the dark current.

$$J = J_{SC} - J_R \exp\left(\frac{eV}{2k_bT}\right) \quad (7)$$

The condition that corresponds to the maximum value V_m of the voltage $\frac{d(JV)}{dV} = 0$ gives:

$$V_m = 0.9V_{OC} - 0.49 \quad (8)$$

Once V_m is known, J_m is deduced using equation (7).

Finally maximum power Pm is directly derived from the product J_mV_m. Although most of the parameters involved in the above equations, namely d_b, d_e, d_w, N_e, N_b, α, β, D_e, $_b$ and v_{th} are known, but the values of the parameters corresponding to the native and irradiation induced defects are not. The concentration N_t, energy level Et and capture cross-section σ of defects have been measured by DLTS [8,12] , the lifetimes have been measured by TRPL. When it comes to the quantitative evaluation of the degradation parameters for cell material the prediction of degradation can be made for any type of cell made of this material, modifying only the emitter and base thicknesses and doping concentrations.

RESULTS AND DISCUSSION

In this study we applied this method to single GaAs cells of different origins under 1MeV electron irradiation, taking into account the calculated values $\tau_{on} = 5x10^{-12}$ s, $\tau_{op} = 5x10^{-8}$ s for carrier lifetimes and the values $k\sigma_n = 1x10^{-12}$ cm and $k\sigma_p = 1x10^{-13}$ cm determined [8] experimentally by DLTS, the other values d_b, d_e, d_w, N_e, N_b were changed for each cell. The results of modellization are given on the (Fig.3)

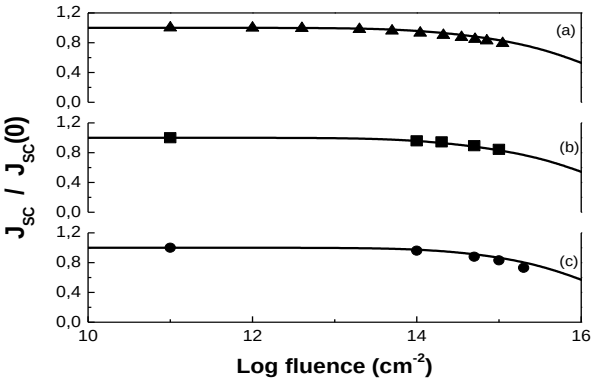

Fig. 3. Degradation of the short circuit current induced by 1 MeV electrons for EEV-Marconi(a), Tecstar(b) and CISE(c) GaAs cell and comparison with experimental data GaAs EEV-Marconi (▲),Tecstar(■) et CISE(●).

We can see when using the same degradation parameters, the same recombination velocity and the same characteristic of native defects in all cases is obtained good agreement between modeling and experimental data (Fig.4)

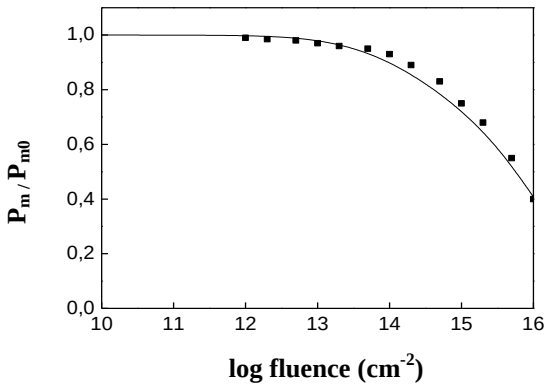

Fig4.Calculated degradation (full line) of the maximum power induced by 1 MeV electrons for NASA GaAs, and comparison with experimental data (■).

The same method was applied for GaAs cell irradiated by protons different energies and results (Fig.5) of modellization shows an excellent fit with experimental data.

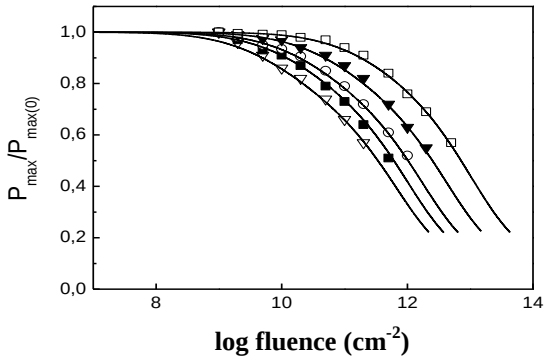

Fig. 5. Degradation (full line) of the maximum power of GaAs (ref.4) versus of the fluence φp of protons energies 300 (∇) keV, 500 (■) keV, 1(o) MeV, 3 (▼)MeV, 9.5 (□) MeV)

Until today, the defects introduced by irradiation in GaInP are not well known ,so in this case we applied the same procedure as for GaAs to calculate the degradation parameters $k\sigma_n = 4x10^{-12}$ cm , $k\sigma_p = 1x10^{-14}$ cm, and the carrier lifetimes $\tau on = 5x10^{-10}$ s, $\tau o_p = 1x10^{-9}$ s.

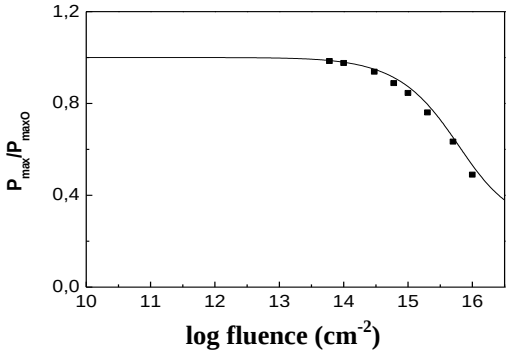

Fig. 6. Degradation (full line) of the maximum power induced by 1 MeV electrons for NRL GaInP cell and comparison with experimental data(■).

Using the same parameters and the principle of equivalence electron-proton we calculate degradation of maximum power for GaInP cell under 3 MeV protons irradiations.

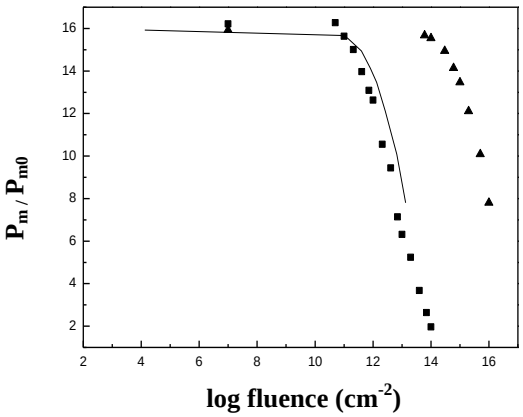

Fig.7. Variation of Pm (full line) for GaInP cell (ref.10) versus the fluence φp of protons energies 3 MeV calculated using the degradations curve of Pm under the 1MeV electron fluence φe (▲) and comparison with the experimental data (■).

Comparison between our results and experimental data shows an excellent fit is obtained in all cases.

CONCLUSION

In this paper, we presented an efficient modeling method to predict degradation of solar cells in space. Using the same degradation parameters we can account reduction of the solar cell efficiency for all types of cells produced of the same material GaAs or GaInP. The difficulty lies in the determination of the recombination velocities, minority carrier lifetimes, defect introduction rate and cross sections for minority carriers trapping on defects. Once these parameters are known for one material it is easy to predict behavior of any solar cell produced of the same material. This method can be extended on 2J and 3J solar cells(13) and also on modeling of degradation for any type of illumination spectrum and in the conditions of low temperature(14).

REFERENCES

[1] J.J.Wysocki, P.Rappaport, (1960).Effect of Temperature on Photovoltaic Solar Energy Conversion. J.Appl.Phys. (31), 571.

[2] J.C.Bourgoin,Zazoui,M.,Irradiation induced degradation in solar cells.Characterization of recombination centers, (2002). Semicond.Sci.Technol. (17), pp.453-460.

[3] D.Pons,J.C.Bourgoin, (1985). Irradiation induced defects in GaAs.J.Phys. C: Solid State Phys. (18), pp.3839-3871.

[4] B.,E.Anspaugh, J.P.L.Pub. GaAs Solar Cell Radiation Handbook, NASA, 1996.

[5] G.P.Summers, M.A.R.J. Walters, E.A.Xapsos, S.R.Burke, Messenger, Shapiro, R.L.Statler, A new approach to damage prediction for solar cells exposed to different radiation, Proceedings of the First World Conference on Photovoltaic Energy Conversion IEEE, 1994.

[6] M.Mbarki, G.C.Sun, J.C.Bourgoin,(2004).Prediction of solar cell degradation in space from the electron-proton equivalence, Semicond. Sci. Tehcnol., (19), 1081-1085.

[7] A.Khan, M.Yamaguchi,J.C.,Bourgoin, K.Ando, J.Takamoto, (2001). Recombination enhanced defect reaction in 1 MeV electron irradiated p GaInP. J.Appl.Phys.89 (8), pp.4263-4268.

[8] M.Zazoui, J.C.Bourgoin,(2002). Space degradation of multijonction solar cell: an electroluminiscence study, Appl.Phys.Lett. 80 (23), pp.4455-4457.

[9] S.Makham,M.Zazoui, G.C.,Sun, J.C.Bourgoin, (2005). Non-empirical prediction of solar cell in space, Semicond. Sci. Technol. (20), 699-704

[10] R.J. Walters, M.A. Xapsos, H.L.,Cotal, S.R.,Messenger, G.P., Summers, P.R.,Sharps, M.L., Timmons, (1998). Radiation response and injectionannealing of p+n InGaP solar cell. Solid-State Electron. 42 (9) pp.1747-1756.

[21] S.M. Sze, (1981) Physics of Semiconductor Devices 2nd ed.Wiley, New York.

[32] A.Khan, M.Yamaguchi, N.Dhamarsu, J.C.,Bourgoin, K.Ando, , J.Takamoto, (2002). Deep level transient spectroscopy analysis og 10 MeV proton and 1 MeV electron irradiation induced defects in p InGaP based solar cells. Japan J.Appl.Phys. (41), pp.1241-1246.

[43] S.Makham, G.C.,Sun, J.C.Bourgoin, , (2010). Modelling of solar cell degradation in space, Solar Energy Materials& Solar Cells. (94), pp.971-978.

[54] S. Makham, H. Samic, G.C. Sun, J.C. Prediction of solar cell behavior for deep space missions. Proceedings of International Symposium on Reliability of Optoelectronics for Space & OPTORAD 2009, Cagliari, Italia, 2009, pp.280-284.

ACKNOWLEDGMENT

The study is selected from *International Symposium on Sustainable Development*, ISSD 2013.

BIOGRAPHIES

Šamić H. was born in Sarajevo, Bosnia and Herzegovina, in 1952. She received the B.S .degree in Physics from the University of Sarajevo, in 1976., M.S. degree in Physics from University of Belgrade in 1988. and the Ph.D. degree in Physics from University of Sarajevo in 1997. From 1995. to 2009. she was a Researcher at the University Pierre and Marie Curie in Paris, France.
From 1977 she has been working at the University of Sarajevo. Today she is a Full Professor at the Faculty of Electrical Engineering, University of Sarajevo. Her research interests include materials physics, semiconductors epitaxial layers growth and applications, medical imaging, solar cells and one-dimensional nano systems.

MAKHAM, S. was born in Casablanca, Morocco in 1975. She received the B.S. degree in physics from the University of Hassan II Mohammedia, in1999., M.S. degrees in physics from the University of Hassan II Ain-chok, in 2001 and the Ph.D. degree in Sciences of engineering from the University, Hassan II Mohammedia, in 2005.
From 2006 to 2012, she was Research engineer in GESEC R&D, in collaboration with University Pierre & Marie Curie. His research interests include semiconductor materials and devices, epitaxial growth and thin film deposition, photovoltaic engineering and x- ray detectors.

Refinement of Calculation Methods for Electrical Load in Industry

O.N. Sinchuk, E.S. Guzov, R.A. Parkhomenko

***Abstract*— An analysis of known and in practice applied methods of electrical load calculation in power supply systems design for iron exploitation and other industry areas is conducted in this paper. Quality and level of discrepancy between the calculated and real values of power supply system parameters are studied. A method of calculation without the shortcomings of methods analyzed is proposed.**

Keywords— **electrical load, calculation methods, power supply**

I. TOPICALITY OF RESEARCH

THE The expected and very much needed improvement regarding economic and technical indicators related to iron exploitation as the raw material for steel industry which is the main participant in Ukraine's GDP formation is directly related with the problem of increasing the effectiveness of power supply systems in mining, including the underground mining facilities [1].

II. MATERIAL AND RESEARCH RESULTS

Many research publications dealing with problem of electrical load calculation for industry and mining have been published [2-5]. These and other works have laid foundations [2] for development in the field of electrical load calculation theory. However, it would not be true to say that this theory of calculation gives a real result that is close enough to actual values, based on the construction schematics of facilities of interest and choice of the parameters for their components.

Exploitation of power supply systems for mining in general, and for iron ore mining in particular is characterized today mainly with significant overestimate in installed power transformers' power in virtually all substations, leading to overestimation regarding the commutator machinery and supply cable cross sections. This situation leads to very big problems, ranging from power losses to supply system protection malfunction. It is result of both objective factors (reduced production and the logically following power consumption) and proactively overestimated values of parameters – electrical loads in the calculation. As we know, all elements of the supply system: transformers, lines, switches etc. are chosen based on the electrical load calculation [2, 3]. A little error in calculation of loads leads to incorrect selection of all components in the supply system, which in turn leads to all sorts of problems. It is not a coincidence that special attention for the calculation of loads has been paid for decades [2-5].

However, the problem of electrical load calculation cannot be considered solved, since significant and non-tolerable discrepancies between calculated and actual loads still exist. Reason for this lies both in imperfection of calculation methods and incorrect use of regulatory factors [4].

III. GOAL OF THIS PAPER

is to analyze methods applied to electrical losses calculation for supply systems in iron mines, measure the quality based on actual and calculated values comparison, as well as to work on suggestions for their improvement.

In mining, as well as other industries, the calculation of electrical loads is usually based on demand factor method and ordered diagrams [2-5]. Let us consider the logic and features of these methods.

Simplest method is one based on demand coefficients, where maximal active power is defined as

$$P_{\max} = \sum_{1}^{n} P_{nom} \cdot c_d \qquad (1)$$

where – is the nominal power of a group of power consumers in same work mode;

I– respective demand coefficient for a group of power consumers in same work mode;

II – number of consumers groups.

It means that the calculation of load is conducted for groups of consumers with same work modes, although in reality we have technological groups with different work modes: workshops, sites, enterprises in general. In other words, it can already be seen that logic of this calculation method. It does not correspond to the structure of power supply system, not to mention a real estimate of work modes among the consumers.

For determination of the demand coefficients one needs to artificially divide consumers into groups with the same mode of operation and know the actual maximum load of these groups, which requires special equipment and a large amount of work. It is not surprising to find out that value of demand coefficients which lie in the essence of this method, have not been updated for over 50 years, so of course the results of calculations of electrical loads by this method are far from

O.N. Sinchuk, is with the Kryvoi Rog National University, str. XXII parts'ezda,11. Ukraine. (e-mail: speet@ukr.net).

reality.

Another flaw of the method using demand coefficients is lack of taking into account the number of consumers, although it is well known that more consumers there are, less the probability that they will work at the same time, hence value of electrical load reduces. To eliminate this shortcoming, another coefficient can be introduced – coefficient of the consumers groups maxima, but its value is taken rather arbitrarily [4].

The flaws of demand coefficient method are partially minimized in the ordered diagrams method, which is recommended in the standards for electrical load calculation in industry [3, 4]. In the context of this method load calculation is performed in two stages: first, determining average load, then going from medium (average) to maximum (peak).

Average active load is defined by:

$$P_{av} = \sum_{1}^{n} P_{nom} \cdot c_u \,, \tag{2}$$

where – coefficient of utility for a group of consumers with the same work mode in the most congested shift.

However, same troubles as in demand coefficient method arise – consumers are divided into groups with same work mode, although in actual power supply scheme technology groups consist of consumers with different modes. Therefore, validation and refinement of the estimated coefficients for use in this method in the process of exploitation is also a problem.

Maximum load:

$$P_{\max} = P_{av} \cdot c_{\max} \,, \tag{3}$$

where–maximum coefficient, found using ordered diagrams as a function of the overall utility coefficient and the equivalent number of consumers.

It's worth noting that ordered diagrams are made for the situation in which demand is random and consumers work independently of each other.

Application in industry is not consistent with reality – energy consumption is a function of the production program and consumers are almost always constrained with a certain production process.

Due to the low accuracy of the ordered diagram method, several authors introduced updates to the method. In [4,5] it is proposed to take the maximum coefficient=1 for consumers with constant load and assume maximum load equal to average in that case, and for the other consumers with variable load maximum coefficient is found using ordered diagrams; in such a manner, an additional division of consumers based on work mode is conducted.

In [4] there is a proposal to use a complex method of electrical load calculation which uses multiple calculation methods at the same time and a data base of analogues as well. Note that the use of the data base of analogues is useful in the application of any of the methods of calculation load, while the use of multiple methods at the same time is not new and does not simplify the task.

The conclusion is that the method of electrical loads calculation and the corresponding estimated coefficients should be focused not on the account of individual consumers and their modes of operation, but on the overall assessment process electricity consumer groups, modes, which are interrelated and being a function of the process.

This corresponds to the structure of real power systems, makes it possible to check the accuracy of calculations and adjust the estimated coefficients using standard instrumentation.

In this regard, statistical calculation methods are of our interest, option from [2] in particular, defining the maximum load as

$$P_{\max} = \left(c_u + \frac{\beta \sigma_*}{\sqrt{n_e}} \right) \cdot \sum_{1}^{n} P_{nom} \,, \tag{4}$$

Where σ_* – relative standard deviation of an effective consumer;

β–probability of maximum (peak) load occurrence (confidence interval), usually in interval 1.5–2.5;

пе – effective number of consumers.

In the above formula (4), the expression in brackets is nothing but the coefficient of demand:

$$c_d = c_u + \frac{\beta \sigma_*}{\sqrt{n_e}} \,. \tag{5}$$

Still, in practice it is a problem to use the demand coefficient in this form, since there is no data on the standard deviations and defining them in production conditions is a complex process.

Let us try to simplify the problem. If a known claim [3] that for a single consumer C_d=1 can be taken, then it holds for $\beta\sigma_*$=1-C_u , so we can write:

$$c_d = c_u + \frac{1 - c_u}{\sqrt{n_e}} \,. \tag{6}$$

This seemingly simple formula well enough expresses the quite complex logic of parameter dependencies in power consumption:

– the main problem of demand coefficient method is solved – effect of the consumers' number is taken into account;

– for a large number of consumers $n_e \rightarrow \infty$, demand coefficient $C_d \rightarrow C_u$, and the maximum power $P_{max} \rightarrow P_{av}$;

– for a small number of consumers $n_{e \rightarrow 1}$, demand coefficient $C_d \rightarrow 1$, and the maximum power $P_{max} \rightarrow P_{nom}$

In this case, calculations of electrical loads by the proposed generalized method requires neither ordered diagrams or standard deviation, or coefficient of utilization for each type of facility. It requires only minimal input information: general utilization rates for technology user groups, and the number of groups, as well as the modes of operation. Then the effective number of consumers is calculated by the known formula [2-5]:

$$n_e = \frac{\left(\sum_1^n P_{nom}\right)^2}{\sum_1^n P_{nom}^2}. \quad (7)$$

For more than 20 consumers, the simplified expression may be used:

$$n_e \approx \frac{2\sum_1^n P_{nom}}{P_{n.\max}}, \quad (8)$$

where $P_{n.\max}$ – nominal power of the consumer with highest power.

In any case while calculating the number of consumers, it has to be remembered that a group of engines working in the same time in a facility is taken into consideration as one motor with the total power given as a sum. On the other hand, consumers in low-power and stand-by modes are not taken into consideration.

For more than 100 consumers, can be taken $C_d = C_u$ [4]. Therefore, for the calculation of electrical loads in 6-10 kV networks average maximal load can be taken as

$$P_{\max} = \sum_1^n P_{av} = \sum_1^n P_{nom} \cdot c_u. \quad (9)$$

Reactive power is determined in a similar fashion as in the ordered diagrams method [2]:

$$Q = \sum_1^n P_{av} \cdot tg\varphi, \quad (10)$$

Where tgφ - power coefficient for respective consumer groups. In order to refine the proposed generalized method and define specific values of coefficients in calculation for design purposes, authors have conducted a series of experimental studies of electrical loads at mining sites of the PJSC "Krivoy Rog's Iron-ore Combine".

During the research, data was collected through electricity meters and daily load graphs were analyzed for three local transformer substations. For the record, meters of active and reactive energy were used, and the power is determined by the number of pulses per unit time

$$P = \frac{N \cdot a}{t}, \quad (11)$$

where N – number of pulses in the considered interval *t*;
a – measured energy for one pulse.

Fig. 1 shows one of the typical daily graphs of local transformer substation load feeding the mining and preparatory site with a total capacity of consumers being

$$\sum_1^n P_{nom} = 215 \text{ kW}. \quad (12)$$

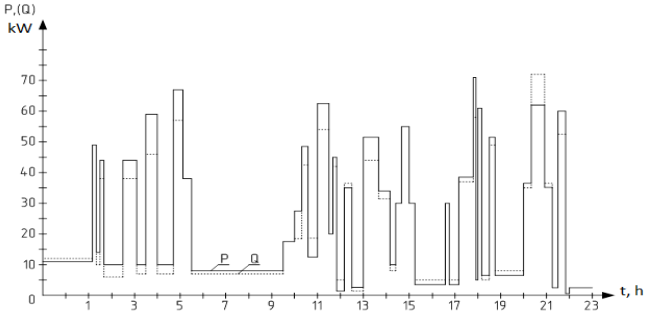

Figure 1 – Daily graph of load for the local transformers substation

In the chart (Fig. 1), one of the typical ones, a three shift working schedule of consumers with sharply varying load can be seen. In some intervals, reactive power (dashed line) is greater than active, indicating short-term overload of the equipment. The average power factor tgφ=0,9.

During the experiment, based on results obtained processing the data (around 20 load charts) following characteristics were determined: peak loads and their duration, mean and standard deviation, coefficients of form, duty fill, demand, utility and power.

Analysis has shown that the transformers' load at the local substations of the state iron ore mines is less than 30% of the installed power. It shows clearly once again the inaccuracy of methods for computation of electrical loads and corresponding coefficients applied.

Experimental data processing and statistical characteristics determination of the daily charts were done using known methods in mathematical statistics, ensuring the required accuracy and reliability of calculations with confidence 0.98 [2].

According to the experimental data, group utility coefficient in different conditions varies between 0.1 and 0.2. For calculation, the maximum value is taken, C_u=0,2.

In calculations, note that the load factor of a single customer is always less than 1 and is usually 0.7-0.9. This allows adjustment of the expression for demand coefficient (6) and presenting it in the form of:

$$c_d = c_u + \frac{0{,}8 - c_u}{\sqrt{n_e}}. \quad (13)$$

If the actual maximum value of utility coefficient C_u=0,2 is used, then the demand coefficient for electrical load calculation in case of iron ore mines can be taken as

$$c_d = 0{,}2 + 0{,}6\frac{1}{\sqrt{n_e}} \quad (14)$$

During the experiment, the power factor tgφ was also determined, which changed in bounds 0.8-0.9 for various sites. For calculations, the maximum value tgφ=0,9 is taken.

To evaluate different electrical load calculation methods comparative calculations were made using ordered diagrams method and the proposed generalized method. Calculation results show that the maximum power calculated with generalized method is 30-40% lower than the one found with

ordered diagrams method and significantly closer to the actual value.

Another detail has to be noted, related to design: the design values of total installed power for the equipment are much higher than actual – in the observed sites, going up to 1.6 times. Given the inaccuracy of calculations it turns out that the transformer capacity is approximately doubled, as seen in reality.

The proposed generalized calculation method for the electrical losses appears to be universal and applicable for all industries and supply systems.

To use the method, it is necessary to know the values of group utility coefficients in the shift with the highest load. This value can be calculated, but it is much more precise if measured in the existing facilities. With a limited number of experiments, in order to account for possible deviations, it is recommended to increase the maximal measurement of the utility coefficient $C_{u.meas}$ by 0.05, meaning that the value of the utility coefficient is

$$c_u = c_{u.meas} + 0{,}05. \quad (15)$$

By the means of modern energy accounting in power supply networks, necessary measurements of the greatest mean loads to determine the actual utilization rates for various technology user groups, departments and companies in general. This will significantly improve the accuracy of calculations and reduce the cost of electricity.

IV. CONCLUSION

1. A new approach to electrical load calculation for technological consumer groups has been made, differing from the known methods by not requiring artificial division in means of working mode, relating to the real structure of power supply systems in mining and other industries.

2. The power values calculated by this generalized method are 30-40% smaller in comparison with other methods applied and significantly closer to their actual values, with the load of power transformers being just around 30%. Judging on this, the power of transformers under the ground can be reduced 1.5-2 times. It is concluded that best choice for transformers' power in district iron ore mines is 250 kVA.

3. A new generalized method of electrical load calculation is based on general efficiency for technological consumers groups, which can be determined with a high degree of precision based on existing energy accounting methods. The method proposed appears to be universal and applicable to all industries and power systems.

ACKNOWLEDGMENT

The study is selected from *International Symposium on Sustainable Development*, ISSD 2013.

REFERENCES

[1] E.K.Babets, L.A.Shtanko, V.A.Salganik, I.E.Melnikova, A.V.Petruhin, C.Ya.Grebenyk, V.O.Tereshenko, E.V.Nusinova Reference book of technical and economic indexes of mining enterprises of Ukraine in 2009 - 2011. – Krivoy Rog: Vidavnichiy dim, 2011. - 329 p. [in Russian]

[2] A.A.Fedorov Basics of power supply of industrial enterprises. – M.: Energiya, 1972. – 321 p. [in Russian]

[3] Reference book on planning of power supply (Under a release of Y.G. Baribin and other) M.: Energiya, 1990. – 285 p. [in Russian]

[4] Kudrin B.I. Power supply of industrial enterprises. – M.: Intermet, 2007. – 501 p. [in Russian]

[5] F.P.Shkrabets, P.G. Pleshkov Basics of power supply. – Kirovograd: KNTU, 2010. – 211 p. [in Ukrainian]

Diagnostic of Inverter Seven Levels Associated with Asynchronous Machine

K. Mendaz, H. Bounoua, M. Feliti, H. Miloudi

***Abstract*— this article presented the diagnostic of the inverters multi levels associates with the three-phase asynchronous squirrel-cage machines. That shows the faults of the switches for each inverter multi levels and their influence on the answers speed and torque.**

***Index Terms*-asynchronous machine, diagnostic, inverters seven levels.**

I. INTRODUCTION

THE voltage source inverters is consisting a non controllable function in the power electronic, it is used in the variable methods application. The strategy obtaining by this technique is based on the study of speed variation in induction machine. The strong evolution of this function was based, on the one hand, on the development of semi-conductor components entirely commendable, powerful, robust and fast, and on the other hand, on the quasi generalized use of the techniques known as pulse width modulated [1, 2].

II. STRUCTURE OF THE INVERTERS HAS SEVEN LEVELS

The three-phase inverter on seven levels with structure studies in this paragraph consists of three symmetrical arms and six sources of equal continuous voltage. Each arm comprises twelve switches of which eights are in series and four in parallel, like two diodes for the zero setting of the arm of the inverter. Each switch is composed of a GTO and of a diode assembled at the head digs as it is shown in the Fig.1 for this inverter; we chose the complementary order defined as follows [2, 4].

$$B_{K5} = \bar{B}_{K3}, \quad B_{K6} = \bar{B}_{K4}, \quad B_{K7} = \bar{B}_{K1}$$

$$B_{K8} = \bar{B}_{K2}$$

K.Mendaz, Sidi Bel Abbes University, department of electrical engineering /Algeria (email:kheiramendez@yahoo.fr)
H.Bounoua, Sidi Bel Abbes University, department of electrical engineering /Algeria (email: hsemmach@yahoo.fr)
M.Feliti, Sidi Bel Abbes University, department of electrical engineering /Algeria (email: FLiti-Med@yahoo.fr)
H.Miloudi, Sidi Bel Abbes University, department of electrical engineering /Algeria (email: al_houssaine@yahoo.fr

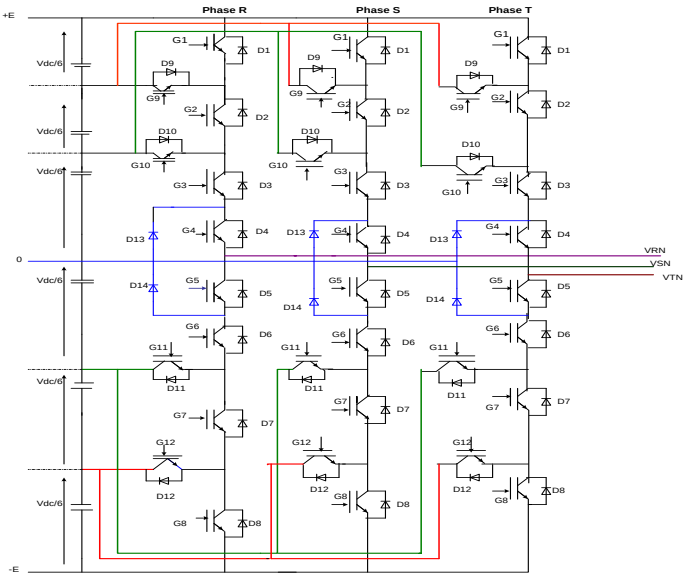

Fig.1 .The inverter seven levels structural

III. VARIOUS CONFIGURATIONS OF AN ARM OF THE INVERTER HAS SEVEN LEVELS

A topological analysis of an arm of the inverter shows seven possible configurations for this last. These various configurations are represented for the Fig.3 to the Fig. 6.
1st configuration: $[1\ 1\ 1\ 1\ 0\ 0\ 0\ 0\ 0\ 0\ 0\ 0]$

To obtained the configuration of the Fig. 3. a. One must order the four switches B_{k1} to B_{k4} with state 1 and the others remain with state 0. Thus, the value of voltage V_{R0} is defined by the equation (1).

$$V_{R0} = (B_3.B_4.)\frac{E}{3} + B_2\frac{E}{3} + B_1\frac{E}{3} = \frac{V_{dc}}{2} \qquad (1)$$

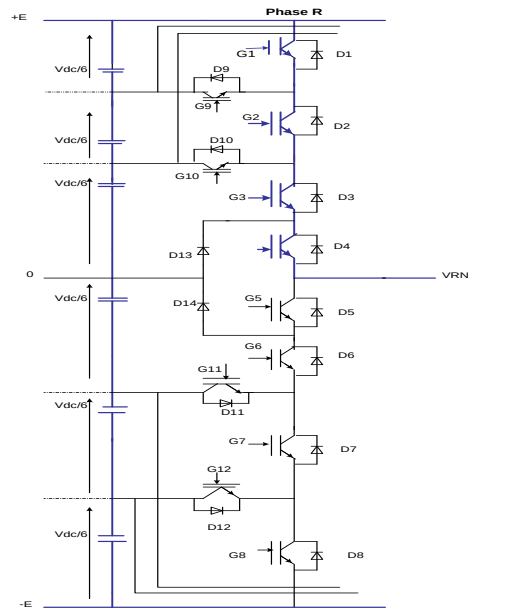

(a)

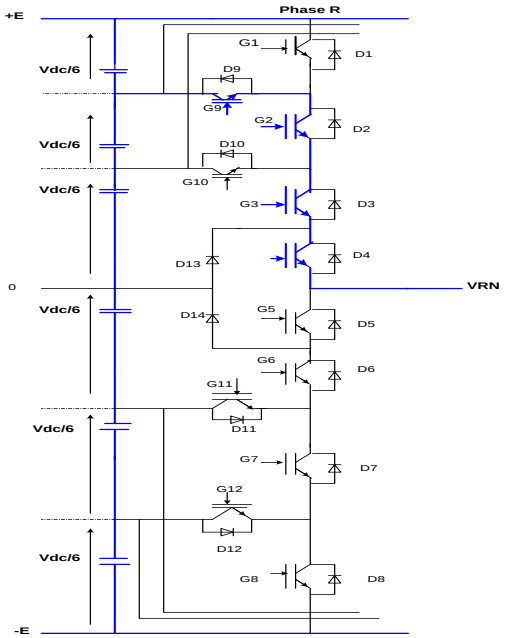

(b)

Fig.3. Different configurations from an arm of inverter on seven levels

2nd configuration: $[0\ 1\ 1\ 1\ 0\ 0\ 0\ 0\ 1\ 0\ 0\ 0]$

This configuration is represented by the Fig.3.b of which the ordering of the following switches B_2, B_3, B_4 and B_9, with the state 1 and others with state 0. The equation (2) gives the value of voltage V_{R0} as follows.

$$V_{R0} = (B_3.B_4.)\frac{E}{3} + (B_2.B_9)\frac{E}{3} = \frac{2E}{3} = \frac{V_{dc}}{2} \qquad (2)$$

3rd configuration:

$[0\ 0\ 1\ 1\ 0\ 0\ 0\ 0\ 0\ 1\ 0\ 0]$

This configuration is represented by the Fig.4.a dowry the ordering of the B_3 switches, B_4 and B_{10} are with state 1 and the remainder of the switches is with state 0. The value of voltage V_{R0} is given by the equation (3).

$$V_{R0} = (B_3.B_4.B_{10})\frac{E}{3} = \frac{E}{3} = \frac{V_{dc}}{6} \qquad (3)$$

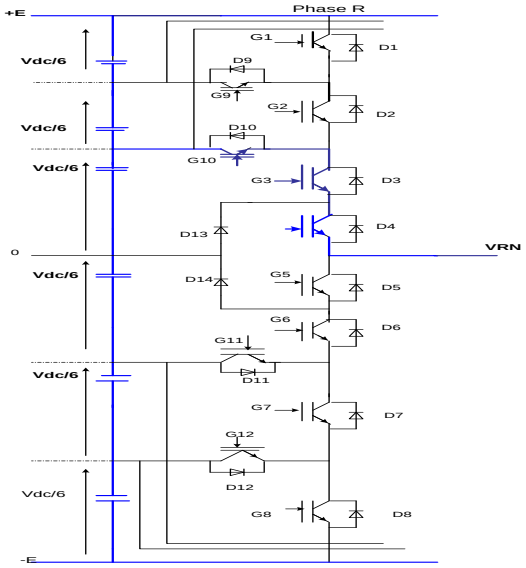

(a)

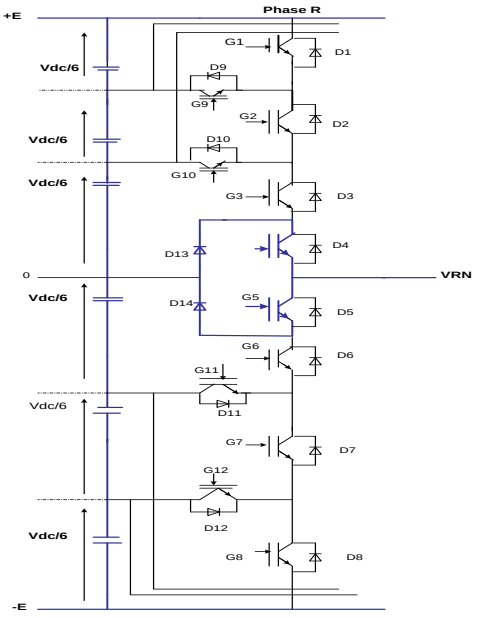

(b)

Fig.4 .Different configurations from an arm of inverter on seven levels

4th configuration :

$[0\ 0\ 0\ 1\ 1\ 0\ 0\ 0\ 0\ 0\ 0\ 0]$

It is the phase of zero setting of the arm of the inverter or the diodes D_{13}et D_{14} return in conduction to ensure the flow of the current. Voltage V_{R0} takes value 0.

5th configuration:

$[0\ 0\ 0\ 0\ 1\ 1\ 0\ 0\ 0\ 0\ 1\ 0]$

The configuration of the Fig. 7.a. has given the switch to state 1 to form the negative part of voltage V_{R0}, this configuration is translated by the equation (4).

$$V_{R0} = (B_5.B_6.B_{11})(-\frac{E}{3}) = -\frac{E}{3} = -\frac{V_{dc}}{6} \quad (4)$$

6th configuration:

$[0\ \ 0\ \ 0\ \ 0\ \ 1\ \ 1\ \ 1\ \ 0\ \ 0\ \ 0\ \ 0\ \ 1]$

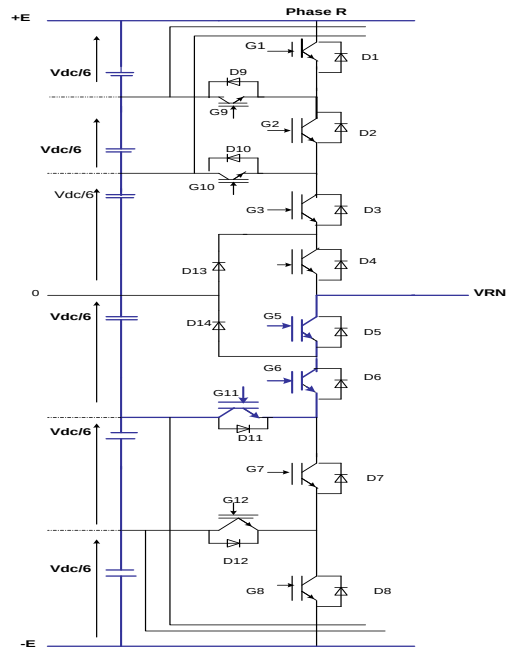

(a)

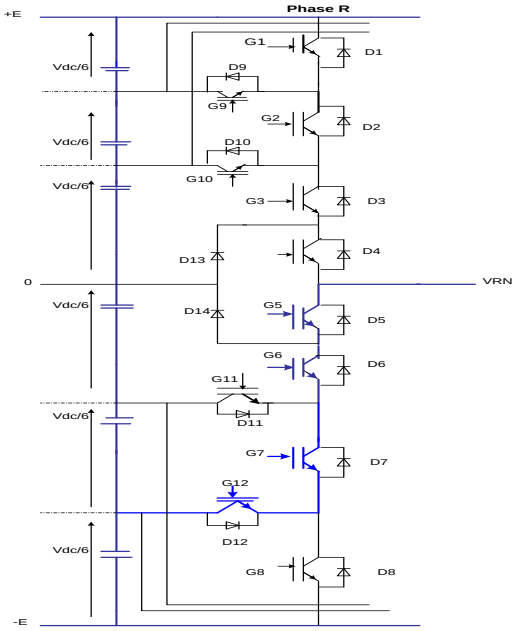

(b)

Fig.5 .Different configurations from an arm of inverter on seven levels

The configuration of the Fig. 5.b requires the ordering of the following switches B_5, B_6, $B_7$and B_{12}; they must be with state 1 and the other with state 0. The equation (5) gives the value of voltage V_{R0} as follows.

$$V_{R0} = (B_5.B_6)(-\frac{E}{3}) + (B_7B_{12})(-\frac{E}{3}) = -\frac{2E}{3} = -\frac{V_{dc}}{3} \quad (5)$$

7th configuration :

$[0\ \ 0\ \ 0\ \ 0\ \ 1\ \ 1\ \ 1\ \ 1\ \ 0\ \ 0\ \ 0\ \ 0]$

This configuration produced - E, the switches in conduction is B_5, B_9, B_7 and B_8 and the remainder of the switches is in a blocked state and tension V_{R0} is given by the equation (6).

$$V_{R0} = (B_5.B_6)(-\frac{E}{3}) + B_7(-\frac{E}{3}) + B_8(\frac{-E}{3}) = -E = -\frac{V_{dc}}{2} \quad (6)$$

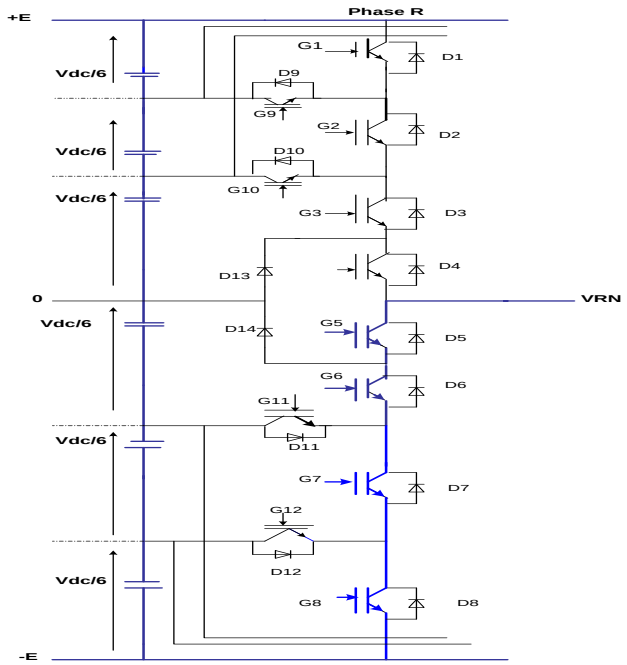

Fig.6. Application of complete and negative voltage.

IV. DIAGNOSTICS FAULTS OF INVERTER MULTI LEVELS

The application domains of the three-phase inverters of voltage most known in industry are undoubtedly that of the electric drives at variable speed. The three-phase inverters, in spite of their qualities, which have pusses to reach thanks to the development of the power electronics, and the use quasi-generalized of the techniques known as of “pulse width modulation”, can present a structural fault such as the fault of closing of the semiconductors. This type of induced dysfunction of the constraints can be damages for the systems of production if the personnel are not informed and that a spurious shutdown is produced. Since, the equipment of protection intervenes only at the last stage of fault; it is thus obvious, that the investment in the field of the

detection of the dysfunctions appears a solution impossible to circumvent [7, 8].

Many faults of the inverters multi levels is detected by using overpressures and the over currents of current system. However, the detection of fault of the elements of commutation is very difficult because the voltage and the current according to each fault of commutation decrease quickly compared to the normal functioning. The disequilibrium of the continuous voltage at the input of the inverter multi levels, as the faults occur, causes serious problem for the protection and the reliability of the system [2, 3, 5].

The fault of K_{17} and k_{12} induces a disequilibrium in the three phases, which translates by the discharge of the lower condensers of the arm R of the inverter five levels [2, 3, 7].

A. DIAGNOSTICS FAULTS OF INVERTER SEVEN LEVELS

In the inverter seven levels, the voltage of phases represented twenty and one levels under symmetrical functional, but their levels of voltage seem to be different with each fault from commutation. The voltage of phase for the positive period has only eight levels because the current of phase crosses the K_{19} switch instead of K_{11} in the state of P (positive). In the event of fault of commutation of K_{110}, the voltage of phase for the positive period has only six levels because the current of phase crosses the K_{110} switch in the state of P (positive). In the event of fault of commutation of K_{13}, the voltage of phase for the positive period has only four levels because the current of phase crosses the K_{14} switch in the P (positive). Consequently, when each fault of commutation occurs, the fictitious voltage differently appeared between them [2, 5, 6, 8].

V. RESULT SIMULATION

For the inverter 7 levels, the Fig.7.b represents the simple voltage V_{an}, the phase voltage V_{ab} is illustrated by the Fig .7.a.

Fig .8 shows also the result of speed and electromagnetic torque were shows that the torque varied then starting to stabilize in the permanent regime.

From the faults of the K_{19} switches of the inverter 7 levels the form of V_{an} voltage and the currents I_{ra}, I_{sa} resulting represented by the Fig.10 and Fig.12 which shows the effect of these faults on disequilibrium of the currents.

The Fig.11 show the conduit of the asynchronous machine, during and after the fault which translates by oscillation of torque and variation speed for the fault of the switch K_{19}.

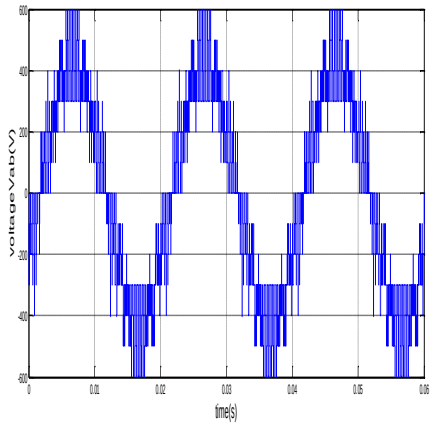

(a)

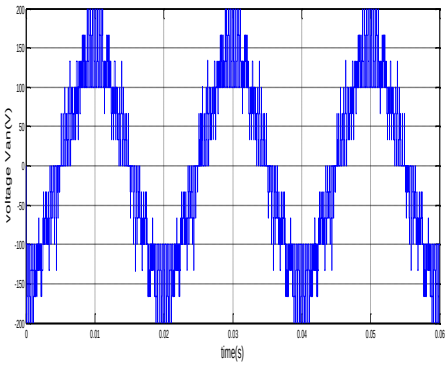

(b)

Fig .7. The voltage results V_{ab} and V_{an} of inverter seven levels without fault.

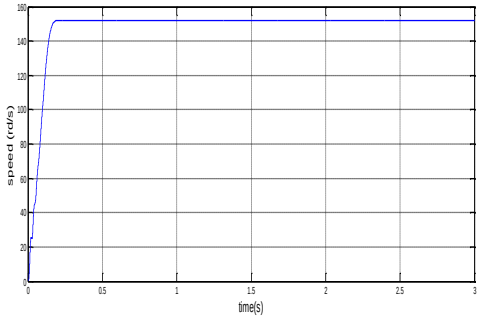

(a)

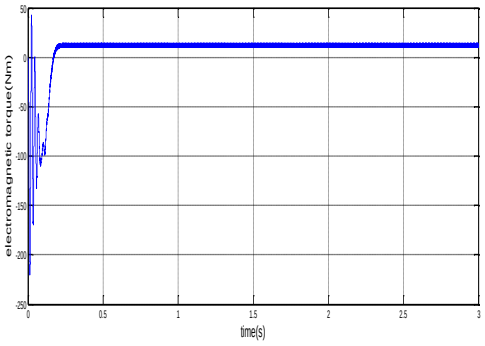

(b)

Fig. 8. Speed, electromagnetic torque results of inverter seven levels without fault

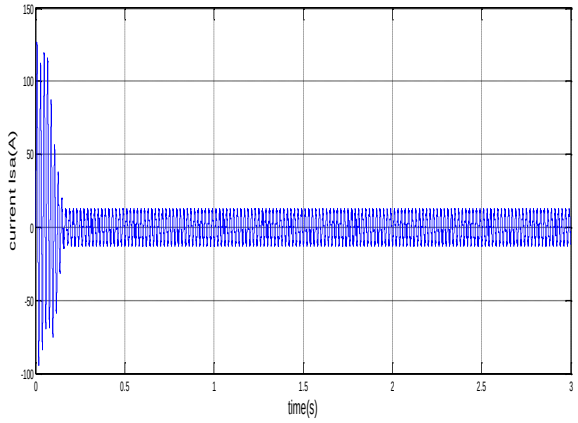

(a)

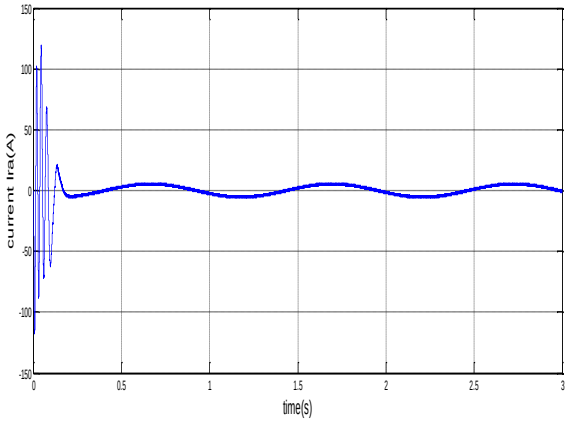

(b)

Fig. 9. The current I_{sa}, I_{ra} result of inverter seven levels without fault

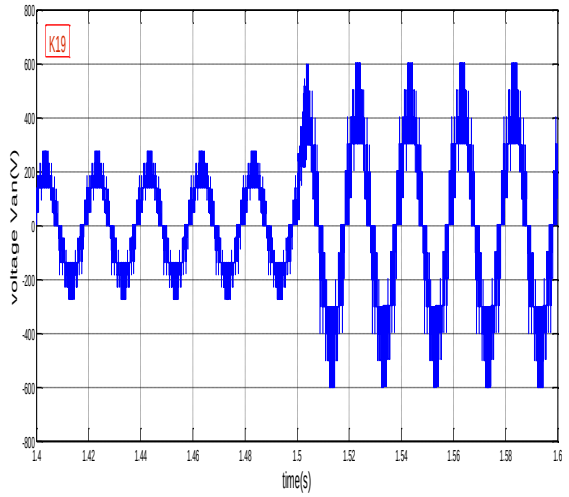

Fig.10 .The voltage results V_{an} of inverter seven levels with fault in switch K_{19} a t (1.4, 1.6)

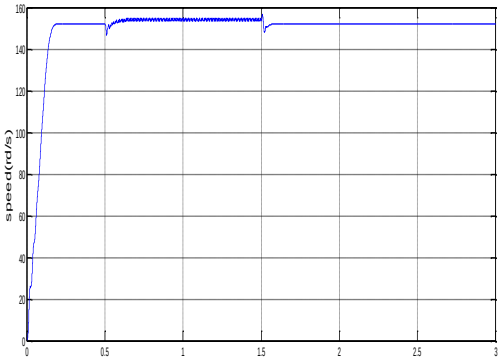

(a)

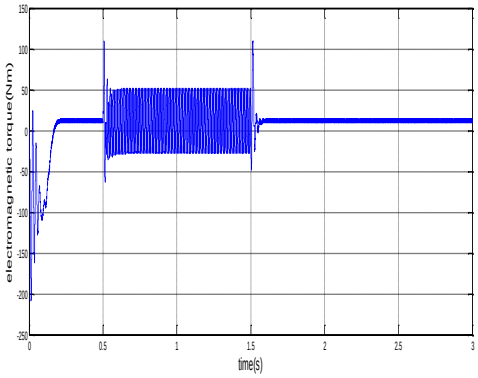

(b)

Fig.11. Speed, electromagnetic torque results of inverter seven levels with fault in switch K_{19} at t (1.4, 1.6)

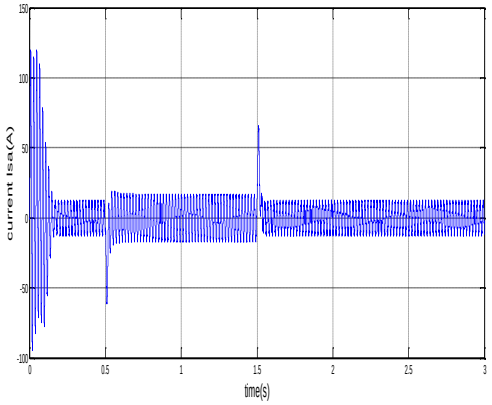

(a)

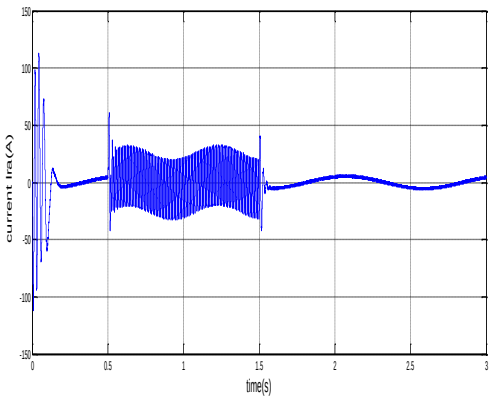

(b)

Fig. 12. the current I_{sa}, I_{ra} result of inverter seven levels with fault in switch K_{19} at t (1.4, 1.6)

VI. CONCLUSION

We developed a new structure of the voltage inverters with three levels, like their principle of operation associated with an asynchronous machine, one notes according to the results obtained a clear improvement of the performances of the unit inverter machine compared to the conventional inverter. Then we elaborate a new functional model of the three-phase inverter with seven levels. The results obtained show well the contribution of the inverters multi levels for the improvement of the performances of the asynchronous machine.

After proposed the diagnosis method of fault of the inverter seven levels which proposes the following advantage, the diagnostic of fault can easily identifies each fault of commutation.

REFERENCES

[1] G. Seguier, F. Labrique " les convertisseurs de l'électronique de puissance," volume 04. , technique et documentation-Lavoisier, 1989.

[2] B. Ouhid, '' la contribution de l'analyse des onduleurs multi niveaux'', mémoire de magister, 2005.

[3] B. Raison, ''Détection et localisation de défaillances sur un entrainement électrique'', Thèse de doctorat, Institut National Polytechnique de Grenoble, France, 2000.

[4] J.N. fiorina, ''onduleurs et harmonique (cas des charges non linaires'', CT édition juin 1992.

[5] J. Sprooten, J.C Maun., ''internal fault analysis of induction machines. Flux magazine'', n° 43 - trimestriel - octobre 2003 - cédrat - cédrat technologies - magsoft corp.

[6] K.Mendaz, ''Développement de nouvelle méthodes numérique pour l'analyse dans la conversion des systèmes électromagnétiques de grande capacité'', Mémoire de magister, université de Sidi Bel Abbes 2008.

[7] Mendaz. K, Bounoua. H, Felliti. M, Day. Z, Diagnostic of Inventer five Levels Associated with Asynchronous Machine, International Conférence on Power electronics and their Applications ICPEA 2013, 6-7 Novembre 2013, Djelfa –Algeria.

[8] Mendaz. K, Bounoua. H, Felliti. M, Diagnostic of inverter three Levels Associated with Asynchronous Machine, International Journal of Engineering Research and Technology IJERT, volume2, Issue9, September 2013.

BIOGRAPHIES

Kheira MENDAZ was born in Ain Temouchent, Algeria, in 1976. He received the engineer in electrical engineering from Djillali Liabes University, Sidi Bel Abbes, Algeria, in 2005, and the M.S degrees in electrical engineering from Sidi Bel Abbes University, Algeria, in 2008; His research interests include high-frequency power conversion, magnetic design, EMI reduction techniques, power electronics and EMC in power converter.

Houria BOUNOUA received the B.S degree in electrical engineering from USTO (Technology Sciences University of Oran), Algeria in 1983, the M.S. and Ph.D degrees in electrical engineering from Sidi Bel Abbes University, Algeria, in 1991 and 2004, respectively. Since 1983, she is a teaching member and involves in research on Numerical command on Power Systems, at Sidi Bel Abbes University (Algeria).

MOHAMED FELITI He received the engineer in electrical engineering from Djillali Liabes University, Sidi Bel Abbes, Algeria, in 2005, and the M.S degrees in electrical engineering from Sidi Bel Abbes University, Algeria, in 2008. His research interests include high-frequency power conversion, magnetic design, EMI reduction techniques, power electronics and EMC in power converter.

HOUSSIN MILOUDI was born in Sidi Bel Abbes, Algeria, in 1982. He received the engineer in electrical engineering from Djillali Laibes University, Sidi Bel Abbes, Algeria, in 2005, the M.S degrees in electrical engineering from Sidi Bel Abbes University, Algeria, in 2008. His main research interests are high-power converters, motor drives, and their application issues.

Hurst Analysis of Induction Motor Vibrations from Aging Process

H. Šiljak and S. Şeker

***Abstract*— Different algorithms for Hurst exponent estimation, namely aggregated variance, absolute moment, Higuchi and Peng method, are applied to eight different vibration signals obtained in induction motor aging process. Signals were obtained with accelerometers during an artificial fluting, thermal and chemical aging process. Applicability of Hurst exponent analysis for motor age detection is discussed based on estimation results. Drop of the exponent value for degraded states with respect to the original state is detected, while no monotonic relationship between subsequent states is found. The anti-persistent nature of vibrations is confirmed.**

Keywords— **Hurst exponents; Long-term dependence; Motor vibration; Aging process.**

I. INTRODUCTION

Hurst exponents (Hurst, 1951) as indicators of long-term dependence have usually been used in case of slow-varying natural processes (Rehman, 2007), traffic (Dong et al., 2010) or finance (Qian and Rasheed, 2004). Recently, in pursuit of new features of vibration signals, Hurst analysis has been conducted on machinery vibrations as well (Lin et al., 2012). While in case of slow-varying processes, Hurst analysis is mainly conducted to determine their nature – whether they are long-term dependent (persistent) or not (anti-persistent), in case of vibrations, the main goal is to get a numerical value and compare it with the same parameter in another condition.

Motivation behind this research is the same – checking whether the Hurst exponent may serve as a basis of simple classification algorithm for detecting motor age on one hand, and whether the vibrations show anti-persistent or persistent nature on the other hand. Another important feature of this research is use of different Hurst exponent estimators and choice of the most suitable one for this particular application.

In the second section, basic concepts are covered, namely experimental setup for motor aging processes, the definition of Hurst exponent and ways of estimating it. Third section presents results of different algorithms for Hurst analysis applied to aging process vibration signals, together with a brief discussion of results. Finally, conclusions are drawn in the last section. Together with conclusions, a suggestion for future research is given, in order to potentially generalize these results.

H. Šiljak, is with the Department of Electrical & Electronics Engineering, International Burch University, 71000, Sarajevo, Bosnia and Herzegovina (e-mail: hsiljak@ibu.ba.edu).

S. Seker is with the Department of Electrical Engineering, Istanbul Technical University, Istanbul, Turkey (e-mail: sekers@itu.edu.tr).

II. BASIC CONCEPTS

For a complete grasp of material covered in this paper, certain introduction to motor aging experimental techniques and the theory of Hurst exponents is needed. Therefore, this section gives the basic information on those topics.

A. Motor aging process experiment setup

An accelerated aging test that had been performed according to IEEE-Std 117 (1974) test procedures gave results in form of eight vibration time series (Erbay, 1999). It was conducted as a combination of fluting, thermal and chemical aging. Namely, fluting aging simulates the electrical discharge from the shaft to the bearing by externally applying shaft current of 27 A at 30 V AC for 30 minutes, while the motor runs with no load.

This procedure was conducted in seven runs before the motor failed in the end of seventh one. This way, eight data sets for motor vibration were collected (first one being the initial case). Sampling frequency is 12 kHz, measurement time 10 s and an anti-aliasing filter at 4 kHz has been applied. Figure 1 shows the first vibration signal record from the experiment.

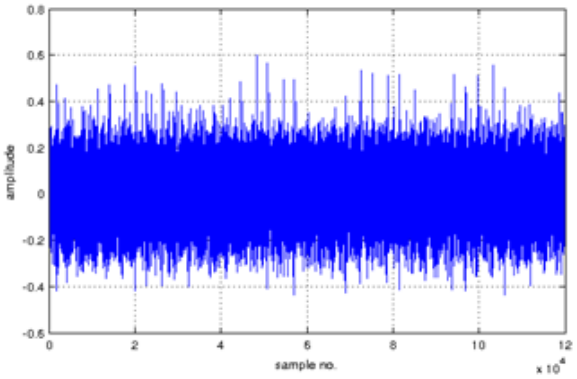

Figure 1. First (out of eight) vibration signal collected in the experiment

B. *The Hurst Exponent*

As defined in (Hurst, 1951), H (Hurst exponent, self-similarity coefficient) is described by the asymptotic relation

$$E\left[\frac{R(n)}{S(n)}\right] \sim n^{H}, n \to \infty \quad (1)$$

Here, $R_{(n)}/S_{(n)}$ is the rescaled range ($R_{(n)}$ is difference between maximum and minimum term in the time series and S(n) is the standard deviation).

For 0.5<H<1 it is said that process has long-range dependence, for H=0.5 it is uncorrelated, while for 0<H<0.5 the process has short-range dependence (Beran, 1994). In simple terms, this means that high values of H correspond to processes which highly depend on previous values and have memory (persistent) while low values express the opposite, being anti-trended (anti-persistent).

Hurst originally used this limit as a method of Hurst exponent calculation in his work on yearly Nile high water (Hurst, 1951).

C. *Methods for Hurst exponent estimation*

There are various methods proposed for Hurst exponent estimation besides the one originally proposed by Hurst (shown in previous subsection). In this paper, four methods are used, namely Aggregated variance, Absolute moment, Higuchi and Peng methods. Description of those methods is adapted from (Taqqu et al., 1995), while the implementations used in this paper are MATLAB functions from (Chen, 2008). All examples of method plots have been made using the vibration data in normal motor state (the one shown in Fig. 1) applying the corresponding MATLAB functions.

First one, Aggregated variance method is using aggregated series

$$X^{(m)}(k) = \frac{1}{m}\sum X(i), k = 1,2,\ldots \quad (2)$$

where m is the block size and k is the block label. Taking sample variance of $X^{(m)}(k)$,k=1,2…within blocks gives an estimate for H since $VarX^{(m)} \sim m^{2H-2}$ as m → ∞. Plotting the logarithm of variance vs logarithm of block size should give a line with slope 2H-2. Example of such procedure is shown in Fig. 2.

Next method is a similar one. For Absolute moment approach, one finds the sum of the absolute values of aggregated series

$$\frac{1}{N/m}\sum |X^{(m)}(k)| \quad (3)$$

which plotted in log scale vs logarithm of block size should give a line with slope . This is shown in Fig. 3 in the same manner as before.

Higuchi method requires calculation of

$$L(m) = \frac{N-1}{m^3}\sum \left\lfloor \frac{N-i}{m} \right\rfloor^{-1} \sum \left| \sum X_j - \sum X_j \right| \quad (4)$$

where N is the time series length and m block size. Since it is $L(m) \sim m^{H-2}$ for m → ∞, slope of the logarithm plot is H-2. This is shown in Fig. 4.

Finally, Peng method does a procedure equivalent to calculating sample variance of the time series. Since $VarX \sim m^{2H}$ for m → ∞, logarithm plot gives a line with a slope of 2H. It is shown in Fig. 5.

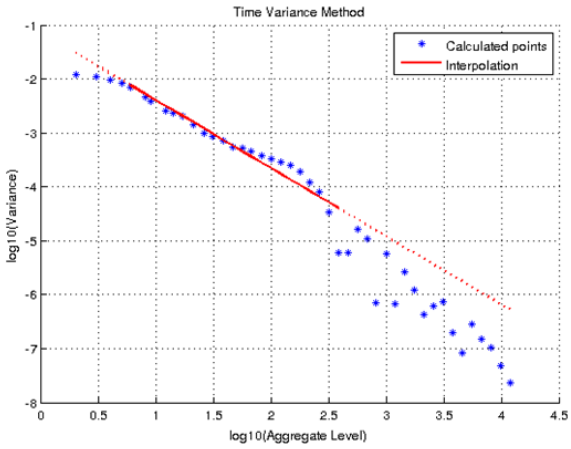

Figure 2. Aggregated variance approach applied to signal in Fig. 1

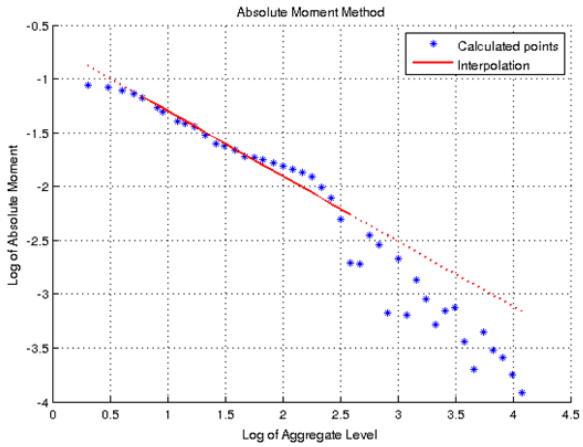

Figure 3. Absolute moment approach applied to signal in Fig. 1

(3)

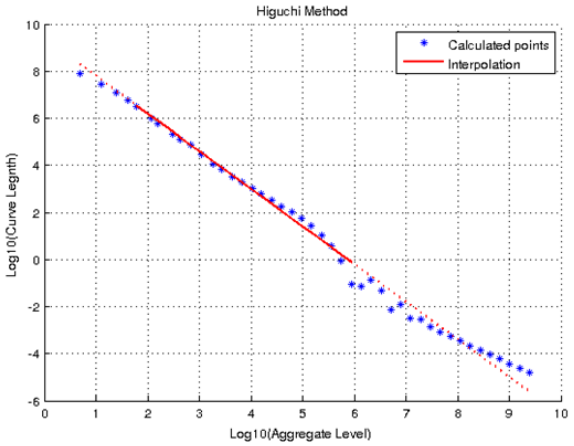

Figure 4. Higuchi approach applied to signal in Fig. 1

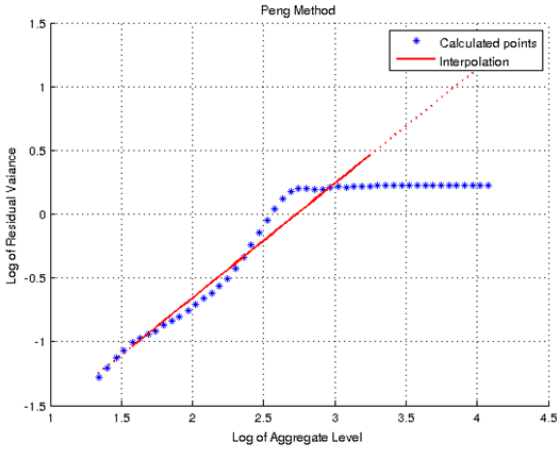

Figure 5. Peng approach applied to signal in Fig. 1

This interval ends when capacitor voltage decreases to zero and output diode turns on.

III. RESULTS AND DISCUSSION

Figure 5 and Table 1 represent the summary of our results. As expected, H < 0.5 regardless of the algorithms and data sets. However, no monotonicity is found – absence of any trend is clearly shown in Figure 5 with a sine-like curve. The numerical values in each of the algorithms do not match. Still, that is not influencing our results, since the overall behavior is the same. By inspection (see Figs 2-5) we may also conclude that the Higuchi method can be taken as the most precise in this case.

Expectation of anti-persistent behavior confirmed here is based on the definition of vibration itself – representing a dynamic excitation whose duration is substantially longer than the response time of the system exposed to it (Harris and Piersol, 2010).

TABLE 1. OBTAINED VALUES FOR HURST EXPONENTS IN DIFFERENT AGING CYCLES AND DIFFERENT METHODS

Algorithm/cycle	0	1	2	3	4	5	6	7
Absolute moment	0.3951	0.3089	0.2892	0.2924	0.3546	0.3689	0.3043	0.3010
Aggregated variance	0.3696	0.2825	0.2695	0.2790	0.3355	0.3451	0.2899	0.2814
Higuchi	0.4016	0.3190	0.2993	0.2997	0.3569	0.3739	0.2980	0.3463
Peng	0.4484	0.3505	0.3296	0.3362	0.3971	0.4101	0.3333	0.2952

It is not clear whether the sine-like behavior of Hurst exponent for different aging cycles is characteristic to these processes in general, but it clearly falsifies a potential hypothesis that Hurst exponent rises or falls monotonically throughout the aging process in whole, although the value of Hurst exponent is clearly lower in every aged state than in original (dataset zero) state, as implied by (Ikizoglu et al., 2010).

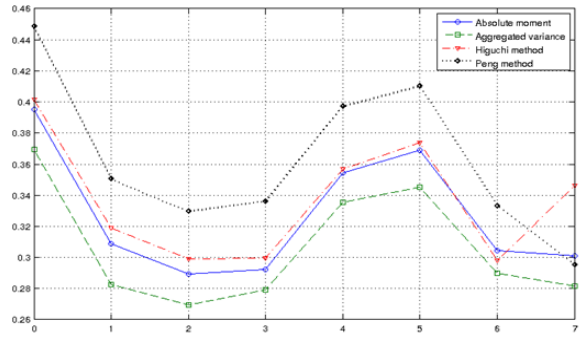

Figure 6. Graphical representation of obtained Hurst exponent values

IV. CONCLUSION

In this paper, Hurst exponents analysis has been applied to motor vibrations with partial success. While the results have shown to be in accordance with theoretical expectations in the matter of signal nature, potential application of this parameter in predictive maintenance does not seem straightforward. Apparent lack of correlation between the motor age and long-term dependence of its vibrations excludes possibility of a simple deduction of its state by looking for the trend of Hurst exponent change. Nevertheless, if similar sine-like behavior is detected for other aging process vibrations, then it may serve as a base of a more complex classification approach. More research has to be conducted in this sense.

V. ACKNOWLEDGEMENTS

The authors thank Prof. B.R. Upadhyaya and his research team at the University of Tennessee, Nuclear Engineering Dept. for allowing use of the experimental data used here.

The study is selected from *International Symposium on Sustainable Development*, ISSD 2013.

REFERENCES

[1] J.Beran, Statistics for Long-Memory Processes. Chapman & Hall, New York, 1994.

[2] K. Q.Dong, P. J. Shang, and H.Zhang, "The Multi-Dependent Hurst Exponent in Traffic Time Series", Applied Mechanics and Materials, vol. 20-23, 2010, pp.346-351.

[3] A. S. Erbay, Multi Sensor Fusion for Induction Motor Aging Analysis and Fault Diagnosis, Ph.D. dissertation, The University of Tennessee, Knoxville, 1999.

[4] H.E.Hurst, Long-term storage of reservoirs: an experimental study. Transactions of the American Society of Civil Engineers, vol.116, 1951, pp.770-799.

[5] Hurst parameter estimate (by Chu Chen) (2008), Last Accessed on Feb 28, 2013. Hyperlink: http://www.mathworks.com/matlabcentral/fileexchange/19148-hurst-parameter-estimate,

[6] S.Ikizoglu, R.Caglar, and S.Seker, "Hurst Parameter and Fractal Dimension Concept for Fault Detection in Electric Motors", Int. Rev. of Electrical Eng. Part A, Vol.5, No.3, 2010, pp. 980-984.

[7] J.Lin, Q. Chen, X. Tian, and F.Gu, "Fault Diagnosis of Rolling Bearings using Multifractal Detrended Fluctuation Analysis and Mahalanobis Distance Criterion", Proc. of the 18th International Conference on Automation and Computing (ICAC), 2012, Loughborough, UK.

[8] B.Qian, and K.Rasheed, "Hurst Exponent and financial market predictability", IASTED conference on Financial Engineering and Applications, FEA 2004, pp.203-209

[9] S.Rehman, "Study of Saudi Arabian climatic conditions using Hurst exponent and climatic predictability index", Chaos, Solitons & Fractals vol.39, no.2, 2009, pp. 499-509.

[10] M. S. Taqqu, V. Teverovsky, and W.Willinger, "Estimators for Long-Range Dependence: An Empirical Study", Fractals, vol.3, 1995, pp. 785-798.

BIOGRAPHY

Harun ŠILJAK (BoEE 2010, MoEE 2012 at University of Sarajevo) is currently a PhD student at the International Burch University Sarajevo. Beside his interest in vibration signal processing, his research interests include generalized functions, random processes, mobile robotics and control theory.

Serhat ŞEKER, was born in Istanbul, Turkey. He received the B.Sc., M.Sc. and Ph.D., degrees from Istanbul Technical University (ITU), Electrical Engineering Department, in 1985, 1988 and 1995 respectively. In 1990 and 1994, he worked with the Nuclear Signal Analysis Group at the Netherlands Energy Research Centre-ECN. Between 1997 and 1998, he joined the University of Tennessee-Knoxville (UT), Nuclear Engineering Department and Maintenance & Reliability Centre (MRC), and studied motor diagnostic problems using artificial intelligent techniques. He is currently working as a professor in Electrical Engineering Department at ITU and his research interests are signal processing, soft computing and condition monitoring techniques.

Hybrid Photovoltaic Inverter for Smart Grids

T. Kupka and M. Patt

***Abstract*— This paper describes a bidirectional solar-battery-grid inverter, its principle and features as well as control functions and recent semiconductors which are used. The device is designed for smart grid applications, where the operator decides about a power and its direction for each active device. The proposed inverter is able to supply power grid by power and phase shift which are defined by superior logic. Or it can take required amount of power from the grid and store it in battery. Stored energy is used later for covering deficiency of solar energy. Solar cells are efficiently driven by MPP tracker and power balancing function ensures maximal usage of all sources.**

Keywords— **Solar inverter, Battery storage, Smart grid, H-bridge, Booster, MPPT, Power balancing**

I. INTRODUCTION

DIRECT solar energy transformation is worldwide spread type of subsidiary energy source. The most widely used system is a connection of string of photovoltaic panels and voltage inverter into the grid. The inverter feeds power network with maximal power, which could the panels currently produce. That leads solar plants to be unstable according to sun shine or clouds, similarly as wind plants depend on wind. Instability problem is often solved by power distribution management covering energy ripple by another source or connection to other network. However, there is growing need to have a solar plant with stable power output.

Another customers of solar industry are small house owners and families. There the need of having stable power source to cover as much their power consumption as possible is recently more and more requested. Currently used design concept of small solar-battery system combines PV and battery inverter and PV charger. Systems are set to cover the house consumption during the day and on the beginning of night. In the time when no energy is available, the consumption is covered by the grid. Example of a sunny day power distribution is shown on Figure 1.

Next step in solar-battery inverter is allowing distribution management to decide what power, its type and direction should be produced or spent by an inverter system. There, the battery could be charged from the grid in case of power surplus.

Tomas Kupka, is with the Department of Electric Drivers and Traction, Faculty of Electrical Engineering, Czech Technical University in Prague, Prague, CZ-16627, Czech Republic. (e-mail: kupkato3@fel.cvut.cz).

Michael Patt, is with Technologienetzwerk Allgäu, Memmingen, D-87700, Germany. (e-mail: michael.patt@tn-allgaeu.de).

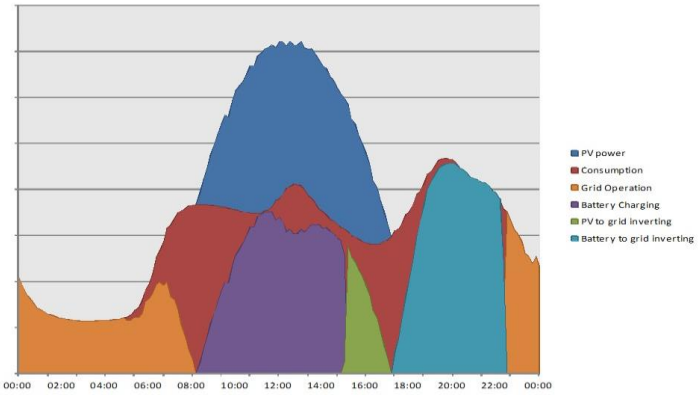

Figure 1: One-day power distribution

II. BLOCK DIAGRAM

The device consists of three active power parts: PV booster, battery buck/boost converter and grid inverter/PFC and control parts: DSP, MUC and boost-driver. Block diagram is shown on Figure 2.

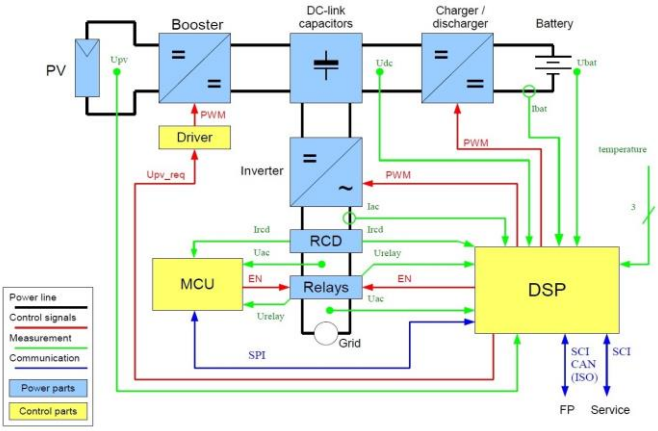

Fig.2. Block diagram

Power parts are connected together or with the ambient by passive power devices: DC-link capacitors, relays, filters and current measurement. Controlling chips, voltage measurements, communication circuits, auxiliary power supply and interconnections represent low power part of system. The most important power blocks will be described below.

A. Photovoltaic booster

The base of this block is one of standard types of DC-DC step-up converter. Its propose is to convert solar voltage to higher DC-link voltage. Value of input voltage is controlled by analog PI regulator according to required value coming out

of central logic (DSP). That function allows Maximal Power Point Tracker (MPPT) to find and set correct operating point.

Two-phase quasi-resonant transition mode construction with interleaved function allows booster to be small and high efficient. Peak efficiency reaches 98.8% in dependence on power and input voltage as shown on Figure 3.

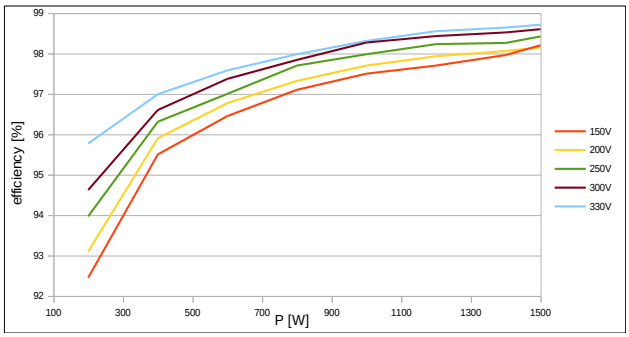

Fig. 3. Efficiency of quasi-resonant PV booster

Smart controlling allows to reach also a high partial load efficiency, because one channel is switched off. The booster works in resonant mode since the PV-input voltage is lower than half of the DC-link voltage as shown on Figure 4, compared to Figure 5 (green – Uds [100V/div]; red – Ugs [10V/div]; violet – current; Udc = 400V).

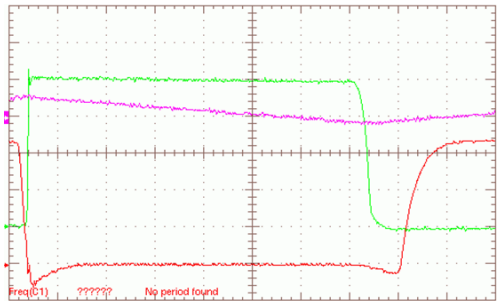

Fig. 4. Resonant switching (Upv=230V)

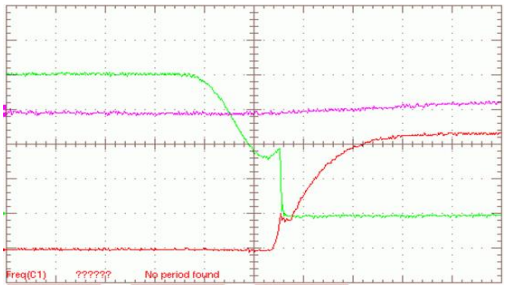

Fig. 5. Non-resonant switching (Upv=356V)

The booster consists of two MOSFETs IPP60R099CPA and two diodes IDP45E60. Both chokes have ferrite cores and additional auxiliary windings for zero-cross detection.

B. Battery buck/boost inverter

This part is responsible for charging and discharging the battery. It's a single leg bidirectional DC-DC converter. Due to the bi-directionality of the converter there are no MOSFETs suitable, because it works in continuous conduction mode (CCM). Discontinuous conduction mode (DCM) is also possible, but it makes the controlling effort higher. The IKW40N65F5 IGBT have been used for the battery buck/boost. They are reaching a peak-efficiency of 95,8 % with a 100V battery and a 390V DC-link voltage. The battery voltage has a high influence on the efficiency like a system related parameter. A 100V battery is comparable with a low voltage PFC. The measured efficiency is shown in Figure 6.

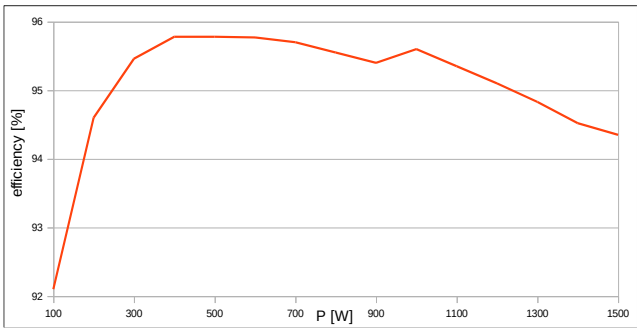

Fig. 6. Battery chopper efficiency for DC-link voltage 390V

C. Grid inverter/PFC

Grid converter is designed as a bidirectional H-bridge inverter with reactive power capability. Optimized high switching frequency provides high efficiency and low dimensions.

There are no MOSFETs suitable if the reactive power is produced by fundamental and if CCM is used. Otherwise the load current commutes from its substart-diode. Even irradiated MOSFETs with fast body-diode have from recent experiences not enough performance because the switching losses are too high. Therefore the IKW40N65F5 IGBTs have been used in H-configuration with bidirectional PWM switching pattern.

D. Common power parts

The rest of power circuit consists of intermediate capacitance, filters, relays, current measurement and interconnections. The DC-Link capacitor current is independent from the reactive power. The complete RMS current is equal to the grid current. The part with double line frequency depends on the modulation index and this depends on the relation between grid voltage and DC-link voltage. Filters make the device free of EMI emissions and a double relay ensures safety of the system, device and operators.

III. CONTROL SYSTEM

Major controlling function is executed by Digital Signal Processor TMS320F2808 from Texas Instruments company. Embedded software contains low hardware controlling functions and measurements as well as higher logic and communication. Firmware calibration and specific settings are stored in a programmable memory. Secondary controller (MCU) is responsible for redundant grid observation and start-up relay check. It communicates with DSP by SPI bus as a

slave, but connecting and disconnecting the relay is autonomic.

DSP is fast and powerful enough to generate and control PWM signals for two inverters, to measure currents, voltages and temperatures including a true RMS measurement of AC values, to keep solar cells in optimal working point by MPPT, to do a simple battery management and to communicate with slave MCU and superior logic. Additionally, software is adjusted to be able to work automatically in one of modes specified in Table 1. Due to this, supervisor need only to set the mode and power and send start command. All other function (MPPT, battery management, power balancing, …) are managed by DSP.

Table 1. Specified woking modes

No.	Mode	Power direction	Set values	Functions
1	Photovoltaic inverter	PV → Grid	ps	MPPT
2	Battery inverter	Battery → Grid	P, ps	BM
3	Grid charger	Grid → Battery	P	BM
4	Photovoltaic charger	PV → battery	P	MPPT, BM
5	Hybrid inverter	PV, Battery → Grid or PV → Grid, Battery	P, ps	MPPT, BM, PB
6	Hybrid charger	Grid → Battery or PV, Grid → Battery	P	MPPT, BM, PB

P – power
ps – phase shift
MPPT – maximal power point tracker
BM – battery management
PB – power balancing

There are three possibilities of controlling the inverter. First two are designed for real operation. It is serial interface (SCI) and CAN bus. Both are optically separated. The thirds serial connection is used for production and service proposes.

A. *Maximal power point tracker (MPPT)*

Maximal power of photovoltaic cell depends on its voltage according to sun shine intensity. There are several algorithms for MPPT implementation (Perturb and Observe, Incremental conductance, etc.). Described inverter uses power derivation feature of photovoltaic panel as is shown on Figure 7. MPPT function works with power derivation similarly to standard Incremental Conductance Algorithm.

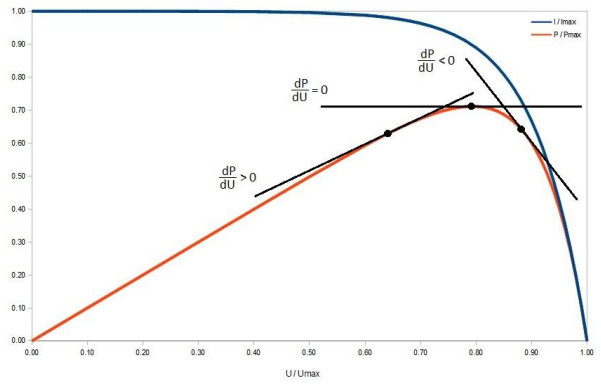

Fig. 7. Power and current to voltage dependance of solar cell

B. *Power balancing*

Base of power balancing system is MPPT, battery management and required power limiter. Maximal power point tracker keeps solar cell working in efficient state, battery charging management decreases the power if the battery is getting full or empty as well as power limiter doesn't allow exceeding required power. These all function together with AC voltage and temperature derater stabilizes the system in simple two-direction modes (1, 2, 3 and 4). For three-direction modes (5 and 6) is necessary to implement additional balancing functions hinted in Table 2.

Table 2. Power balancing logic background

	Priority	4	3	3	2	1
	Event	Normal operation	BM power limitation	Required power exceeded	AC voltage limit	Temperature limit
PV inverter	Booster	MPPT	-	Control P-required	Control P-AC limit	Control P-temp. limit
	Battery bridge	-	-	-	-	-
	Grid bridge	Follow PV	-	Follow PV	Follow PV	follow PV
Bat. inverter (discharging)	Booster	-	-	-	-	-
	Battery bridge	Control P-required	Control P-BM limit	Control P-required	Control P-AC limit	Control P-temp. limit
	Grid bridge	Follow Battery	Follow Battery	Follow Battery	Follow Battery	Follow Battery
Grid Charger (charging)	Booster	-	-	-	-	-
	Battery bridge	Follow Grid	Follow Grid	Follow Grid	Follow Grid	Follow Grid
	Grid bridge	Control P-required	Control P-BM limit	Control P-required	Control P-AC limit	Control P-temp. limit
PV Charger (charging)	Booster	MPPT	Control P-BM limit	Control P-required	Control P-AC limit	Control P-temp. limit
	Battery bridge	Follow PV	Follow PV	Follow PV	Follow PV	Follow PV
	Grid bridge	-	-	-	-	-
Hybrid Inverter	Booster	MPPT	MPPT	MPPT or Control P-required (if battery is full)	MPPT or Control P-AC limit (if battery is full)	MPPT or Control P-temp. limit (if battery is full)
	Battery bridge	Charge (if Ppv > P-required), Discharge (if Ppv < P-required)	Decrease P (if discharging), Increase P (if charging)	Decrease P (if discharging), Increase P (if charging)	Decrease P (if discharging), Increase P (if charging)	Decrease P (if discharging), Increase P (if charging)
	Grid bridge	Follow PV and Battery	Follow PV and Battery	Follow PV and Battery	Follow PV and Battery	Follow PV and Battery
Hybrid Charger	Booster	MPPT	Decrease P	Decrease P	Decrease P	Decrease P
	Battery bridge	Follow PV and Battery	Follow PV and Battery	Follow PV and Battery	Follow PV and Battery	Follow PV and Battery
	Grid bridge	Control P-required	Control P-required, Decrease P (if PV disabled)	Control P-required	Control P-required, Decrease P (if PV disabled)	Control P-required, Decrease P (if PV disabled)

IV. CONCLUSION

The paper described one of recent solar inverters, its design, features and technology. Maximal power point tracking and power balancing problematic was mentioned too.

Further development will be focused to use the inverter in fully island mode. That device could be used like power source in places without energy connection or like an emergency power supply in power line defection.

ACKNOWLEDGMENT

The study is selected from *International Symposium on Sustainable Development*, ISSD 2013.

REFERENCES

[1] M.Patt,(2008). Eigenschaften vontransformatorlosen Photovoltaikwechselrichtern. Proceedings VDE Kongress München

[2] M.A.Elgendy, B.Zahawi, & D.J.Atkinson, (2012). Low Cost MPPT Algorithms for PV Application: PV Pumping Case Study. Newcastle University presentation

BIOGRAPHIES

Tomas Kupka received the master degree in electrical engineering from the Brno University of Technology, Czech Republic, in 2006. Presently he continues education the Ph.D. degree in on Czech Technical University in Prague, Czech Republic, with planed graduation in 2015. He also works in design-house company Finepower GmbH in Ismaning, Germany. His domains are controlling systems for power application.

Michael Patt received the doctor degree in power electronic from the Helmut Schmidt University in Hamburg, Germany. Since 2012 he holds a professorship on Technologienetzwerk Allgäu, Memingen, Germany. The scale of his interest consists of power electronic for voltage and current inverters in various applications.

Photovoltaic Power Control Using MPPT and Boost Converter

A.Attou, A.Massoum and M.Saidi

***Abstract*—The studies on the photovoltaic system are extensively increasing because of a large, secure, essentially exhaustible and broadly available resource as a future energy supply. However, the output power induced in the photovoltaic modules is influenced by an intensity of solar cell radiation, temperature of the solar cells. Therefore, to maximize the efficiency of the renewable energy system, it is necessary to track the maximum power point of the input source. In this paper, a new maximum power point tracker (MPPT) using Perturb & Observe algorithm is proposed to improve energy conversion efficiency. Maximum power point tracking is an important function in all photovoltaic (PV) power systems. The simulation results show that the proposed MPPT control can avoid tracking deviation and result in improved performance in both dynamic response and steady-state.**

Index Terms— **Maximum power point tracking (MPPT), photovoltaic (PV) power system, maximum power point (MPP), switching mode DC-DC converter, switching duty cycle, Perturb & Observe control.**

I. INTRODUCTION

SOLAR energy is one of the most important renewable energy sources. Compared to conventional non renewable resources such as gasoline, coal, etc... , solar energy is clean, inexhaustible and free.

Photovoltaic (PV) generation is becoming increasingly important as a renewable source since it offers many advantages such as incurring no fuel costs, not being polluting, requiring little maintenance, and emitting no noise, among others. The photovoltaic array is an unstable source of power since the peak power point depends on the temperature and the irradiation level. A maximum peak power point tracking is then necessary for maximum efficiency [3,5].

The V-I and V-P characteristic curves specify a unique operating point at which maximum possible power is delivered. At the MPP, the PV operates at its highest efficiency. Therefore, many methods have been developed to determine MPPT [5].

In this work, a maximum power point tracker for photovoltaic panel is proposed. dP / dV and variation of duty cycle (ΔD), are used to generate the optimal MPP converter duty cycle, such that solar panel maximum power is generated under different operating conditions. A photovoltaic system including a solar panel, a DC-DC converter and a resistive load is modeled and simulated [3].

Amine ATTOU, is with the electrical engineering Department, Faculty of Technologie, Djillali Liabes University, Sidi-bel-Abbes, 22000, Algeria. (e-mail: attouamine@yahoo.fr).

Ahmed MASSOUM, is with the electrical engineering Department, Faculty of Technologie, Djillali Liabes University, Sidi-bel-Abbes, 22000, Algeria. (e-mail: ahmassoum@yahoo.fr).

Mossaab SAIDI, is with the electrical engineering Department, Faculty of Technologie, Djillali Liabes University, Sidi-bel-Abbes, 22000, Algeria. (e-mail: saidimoss@hotmail.fr).

II. MATHEMATICAL MODEL

The building block of PV arrays is the solar cell, which is basically a p-n semiconductor junction, shown in Fig.1. The V-I characteristic of a solar array is given by Eq. (1)

$$I = I_{sc} - I_o\left\{exp\left[\frac{q(V + R_s I}{nkT_k}\right] - 1\right\} - \frac{V + R_s I}{R_{sh}} \qquad (1)$$

Where:

- V and I represent the output voltage and current of the PV, respectively.
- R_s and R_{sh} are the series and shunt resistance of the cell.
- q is the electronic charge.
- $I_{SC}$is the light-generated current.
- I_o is the reverse saturation current.
- n is a dimensionless factor.
- k is the Boltzman constant, and T_k is the temperature in ^oK.

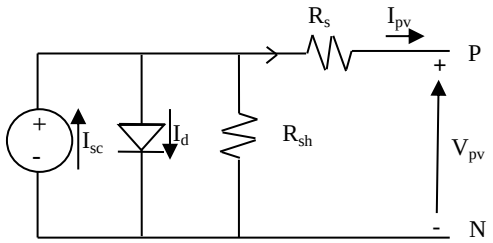

Fig.1 Equivalent circuit of PV array.

Equation (1) was used in computer simulations to obtain the output characteristics of a solar cell, as shown in Fig. 2.

This curve clearly shows that the output characteristics of a solar cell are non-linear and are crucially influenced by solar radiation, temperature and load condition [2,5]. Each curve has a MPP, at which the solar array operates most efficiently.

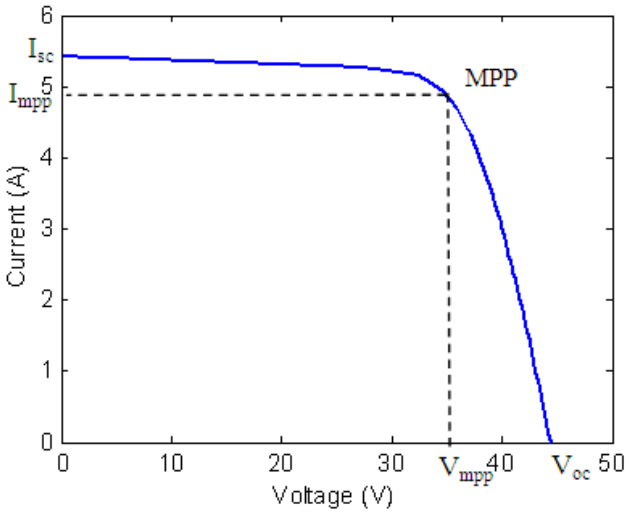

Fig. 2V-I characteristic of a solar cell.

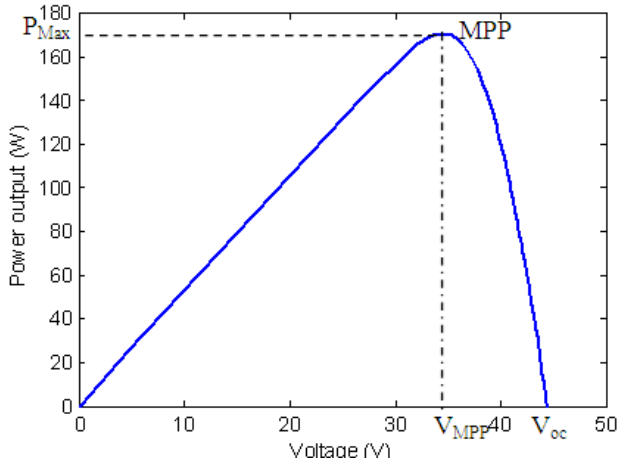

Fig. 3 V-P characteristic of a solar cell.

III. BOOST CONVERTER

Consider a boost type converter connected to a PV module with a resistive load as illustrated in Fig. 3.

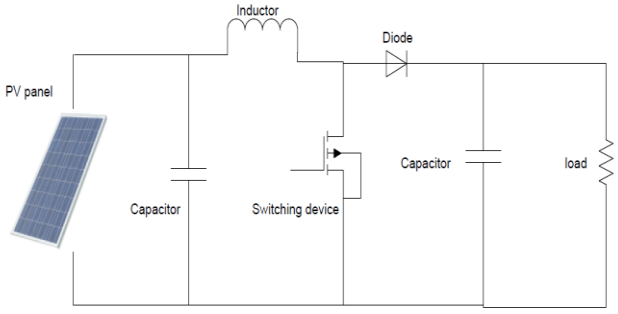

Fig. 4 Boost converter.

The power switch is responsible for modulating the energy transfer from the input source to the load by varying the duty cycle D [2-4].

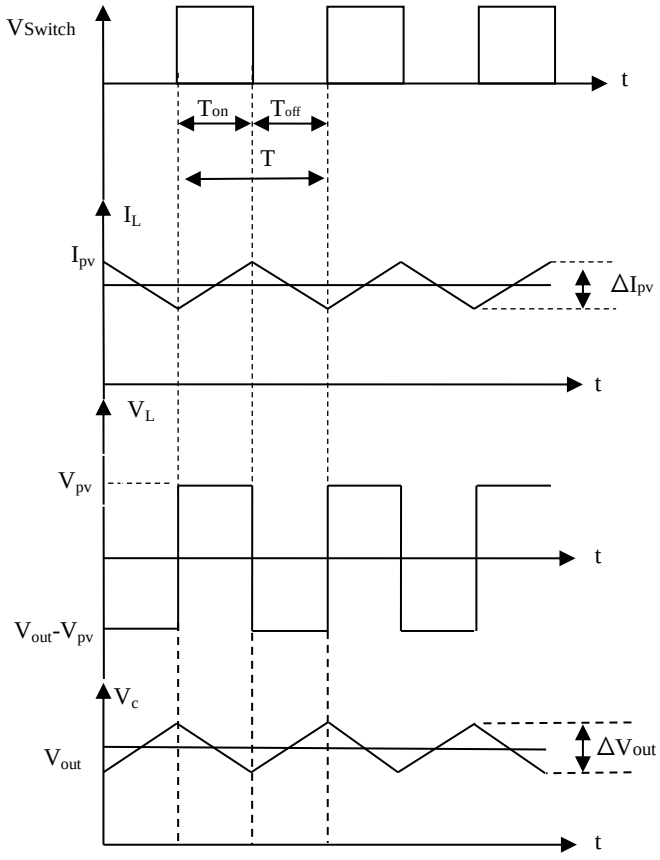

Fig. 5 Typical forms wave of boost converter.

$$V_{pv}\ t_{on} = (V_{out} - V_{pv}) \cdot t_{off} \quad (2)$$

And,

$$V_{out} = \frac{t_{on}+t_{off}}{t_{off}} V_{pv} \quad (3)$$

Where;

$$T = t_{on} + t_{off} \quad (4)$$

The report $\frac{t_{on}}{T}$ is called the duty cycle α and therefore

$$\alpha = \frac{t_{on}}{T} \quad (5)$$

From equation (3), the voltage release can be derived:

$$V_{out} = \frac{1}{1-\alpha} V_{pv} \quad (6)$$

where :

- V_{out} : isthe output voltage.
- V_{pv} : is thevoltageinput (solar cell).
- t_{on} : is the durationof time whenthe switch is closed.

IV. PROPOSED MPPT ALGORITHM

Maximum power point tracking, or MPPT, is the automatic adjustment of the load of a photovoltaic system to achieve the maximum possible power output. PV cells have a complex relationship between current, voltage, and output power, which produces a non-linear output. This output is expressed as the current-voltage characteristic of the PV cell.

Constant fluctuations in external variables such as temperature, irradiance, and shading cause constant shifts of the I-V curve upwards and downwards. A change in temperature will have an inversely proportional effect on output voltage, and a change in irradiance will have a proportional affect on output current [1].

The maximum power point tracking (MPPT) canbeaddressed by different ways, for example: fuzzy logic, neural networks and pilot cells. Nevertheless, the perturb and observe (P&O) and Incremental Conductance (INC) techniques are widely used, especially for low-cost implementations.

The P&O MPPT algorithm is mostly used, due to its ease of implementation. It is based on the following criterion: if the operating voltage of the PV array is perturbed in a given direction and if the power drawn from the PV array increases, this means that the operating point has moved toward the MPP and, therefore, the operating voltage must be further perturbed in the same direction. Otherwise, if the power drawn from the PV array decreases, the operating point has moved away from the MPP and, therefore, the direction of the operating voltage perturbationmust be reversed [6].

The MPP tracker operates by periodically incrementing or decrementing the solar array voltage. If a given perturbation leads to an increase (decrease) the output power of the PV, then the subsequent perturbation is generated in the same (opposite) direction. In Fig.6, set Duty out denotes the perturbation of the solar array voltage, and Duty+ and Duty_ represent the subsequent perturbation in the same or opposite direction, respectively[2,5].

In Fig. 6 it is given a flowchart witch describe the P & O technique:

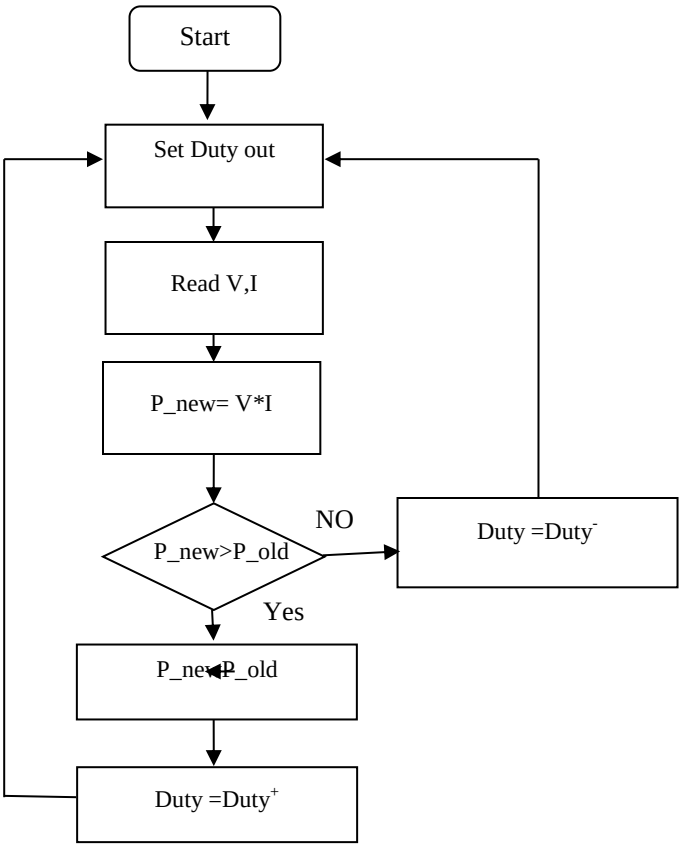

Fig. 6Flow chart of the P&O algorithm.

V. SIMULATION RESULTS

The modeling and simulation of the system (photovoltaic generator, boost converter and MPPT algorithm P&O) is then made with Matlab/Simulink software to validate the control strategy and evaluate the performance of the system. Fig. 7 represents the model used in the simulation.

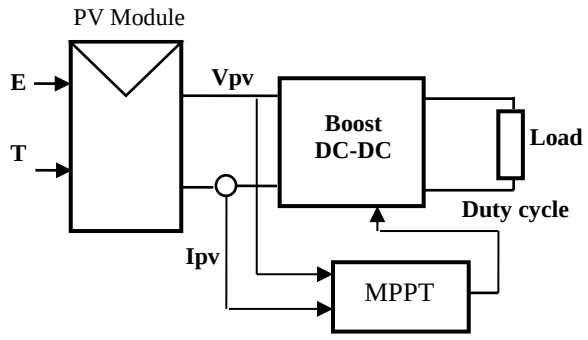

Fig. 7 System simulation model .

Fig.8 shows thesimulation results. We show that theMPPTcontrolforces the system to work optimally at all times around the maximum power point.

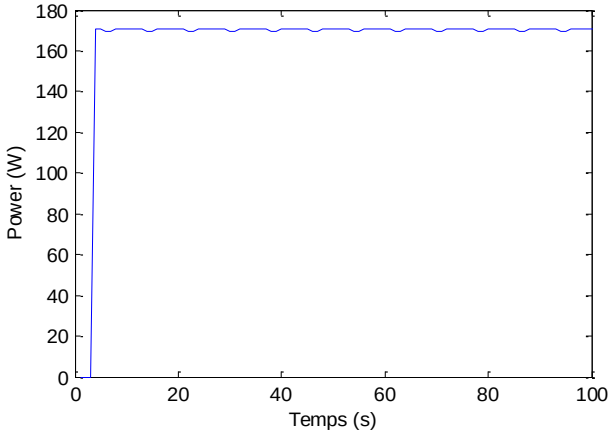

Fig. 8 PV-Output Power of with MPPT.

The change in level of irradiance and temperature are presented in order to show the robustness. First, the use of varied levels of irradiation is presented in the Fig. 9.

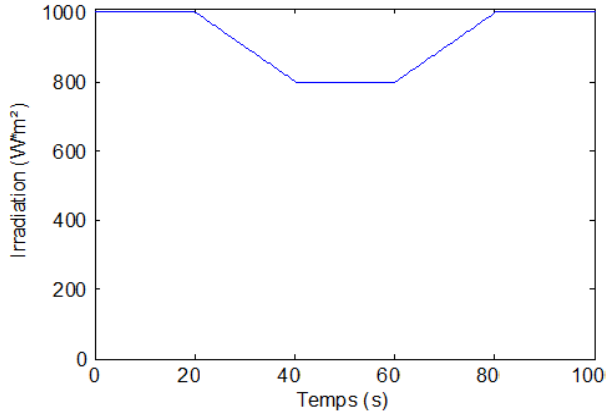

Fig. 9. The irradiation for many levels expressed in Wm^2.

For these levels of irradiation, the following figure represents the maximum power in the output of PV array.

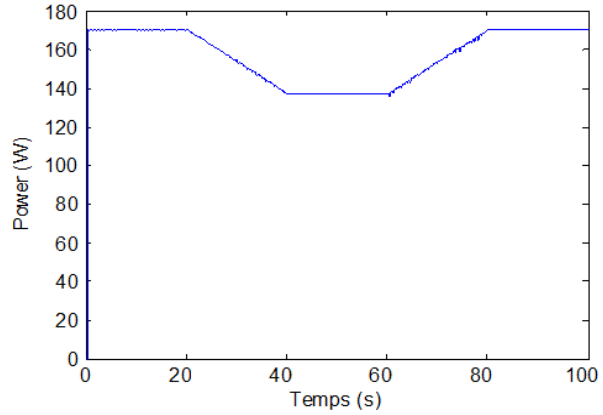

Fig. 10Power in the output of the PV array.

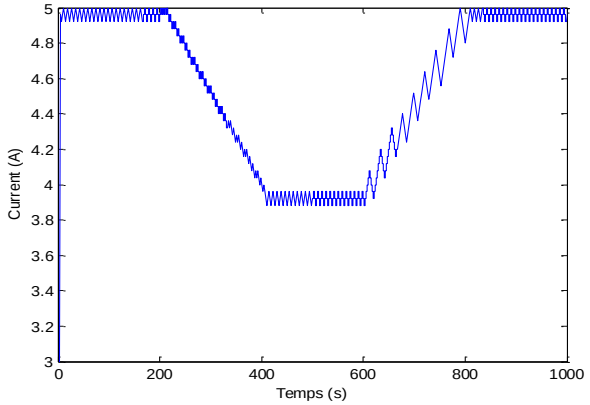

Fig. 11 Plot of Cuurent Output of PV panel.

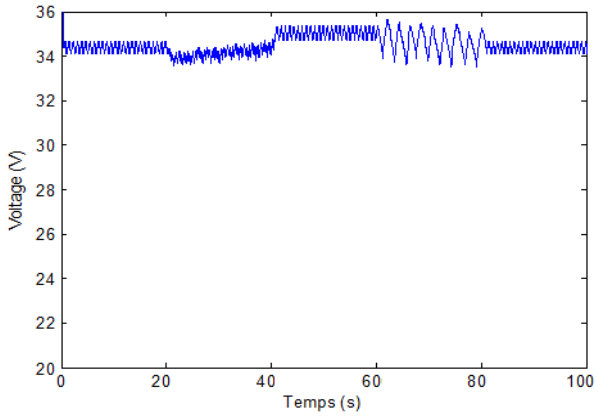

Fig. 12 Plot of Voltage Output of PV panel.

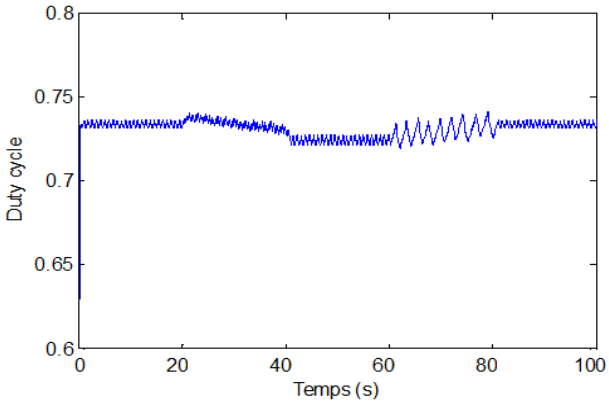

Fig. 13.Simulated duty ratio response of a PV system.

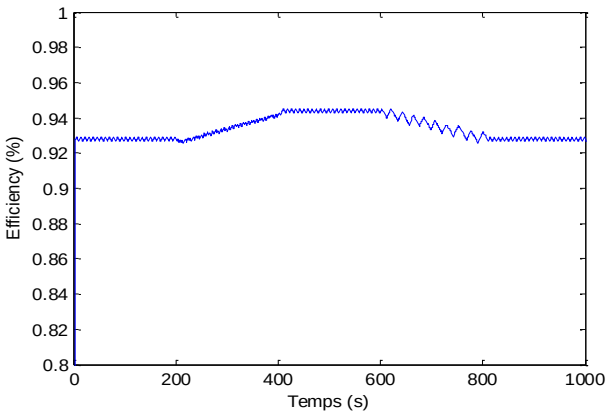

Fig. 14. Simulated the Efficiency response of a PV system.

In Fig.10, the simulation results of the output power of the PV panel using Perturb an Observe method controller is reported, so we can say it is shown that the P&O method, when properly optimized, leads to an efficiency which is equal to 94 % as shown in Fig. 13. We note that a method of P & O show converge to the value of MPP at steady sate. However, when the irradiation changes rapidly the P & O controller shows a better time response method.

IV. CONCLUSION

An energy-efficient fast-tracking MPPT circuit PV energy harvester is presented in this paper. Firstly the characteristics of PV system and vector mathematical model are presented.

The MPPT strategy based on Perturb & Observe method is proposed. The results obtained from simulation employing

P & O approach show the effectiveness of the proposed power tracking and control strategies with quick power tracking response and well direct current output.

ACKNOWLEDGMENT

The study is selected from *International Symposium on Sustainable Development*, ISSD 2013.

REFERENCES

[1] A. Barchowsky, J. P. Parvin, G.F. Reed, M. J. Korytowski, B.M. Grainger, "A Comparative Study of MPPT Methods for Distributed Photovoltaic Generation", Conference Publications, Innovative Smart Grid Technologies (ISGT), 2012 IEEE PES, 2012, pp.1-7.

[2] M.A.Elgendy, B. Zahawi, D.J. Atkinson, "Evaluation of perturb and observe MPPT algorithm implementation techniques", Power Electronics, Machines and Drives (PEMD 2012), 6th IET International Conference, IEEE Publication, March 2012, pp.1-6.

[3] A. Chouder, F. Guijoan, S. Silvestre, "Simulation of fuzzy-based MPP tracker and performance comparison with perturb & observe method", Revue des Energies Renouvelables, vol.11, no.4, 2008, pp.577-586.

[4] M. Arrouf, Optimization of Inverter, Motor and Pump Connected with a Photovoltaic Cell, Ph.D. thesis, University of constantine, Algeria, 2007.

[5] J.A. Jiang, T. H. Huang, Y.T. Hsiao and C.H. Chen, "Maximum Power Tracking for Photovoltaic Power Systems", Tamkang Journal of Science and Engineering, vol. 8, no 2, 2005, pp. 147-153.

[6] N. Femia, G. Petrone, Giovanni Spagnuolo, and M. Vitelli, "Optimization of Perturb and Observe Maximum Power Point Tracking Method", IEEE Transactions on Power Electronics, vol.20, no.4, 2005, pp.963-973.

BIOGRAPHY

Amine ATTOU, he was born in Sidi-bel-Abbes City, in 1987. He received the L.S. and M.S. degrees in electrical engineering from the University of Djillali Liabes, Sidi-bel-Abbes in 2011. He is a member in Intelligent Control Electrical Power System Laboratory (ICEPS).

Ahmed Massoum, he was born in M'sirda Fouaga, Tlemcen, Algeria, in 1959. He received his BS degree in electrical engineering from the Electrical Engineering Institute (INELEC) of Boumerdes 1985 and the MS degree from the Electrical Engineering Institute of Sidi-bel-Abbes University in 2004 where he is currently Professor of electrical engineering. He is a member in Intelligent Control Electrical Power System Laboratory (ICEPS).

Mossaab SAIDI, h**e** was born in SIDA City, in 1988. He received the L.S. and M.S. degrees in electrical engineering from the University of Djillali Liabes, Sidi-bel-Abbes in 2011. He is a member in Intelligent Control Electrical Power System Laboratory (ICEPS).

Sequence Partitioning and Compression Rate

B.B. Alagoz and H.Z. Alisoy

***Abstract*— In the lossless data compression, the process of splitting a data sequence into appropriate subsequences has a substantial role in improving compression rate. This study theoretically investigates effects of data sequence partition on the overall compression rate of data sets. For this proposes, we show that it is always possible to find a partition of data sequence such that the entropy rate at each subsequence is lower than entropy rate of original sequences. This motivates our work to figure out the overall compression rate of the partitioned data sequences. Then, the effects of sequence partitioning on overall compression rate are discussed to explore an optimal partitioning strategy. Finally, an optimization problem for the optimal partitioning of a data sequences is stated for future works.**

***Index Terms*— Information theory, entropy rate, compression rate, Shannon limit.**

I. Introduction

SHANNON established a fundamental limit to lossless data compression in 1948. This limit was stated depending on entropy rate. He revealed that it was possible to compress information coming from a data source, in a lossless manner, with a compression rate close to the entropy rate of data source by using an coding method [1-2]. The entropy rate indeed depends on the statistical nature of the data sources. As the statistical order of a data source increases, the entropy rate of the source decreases. In this way, a better compression rate can be achievable by applying appropriate coding techniques. Today, the most popular coding methods applied in practice are Huffman Coding and Lempel-Ziv Coding [3-5].

The process of data set partitioning is one of the primary tasks effecting performances of coding schemes. In practice, several coding strategies were practically developed for splitting and coding a data sequence to achieve a lower compression rates [6-10]. For instance, a refined partition providing minimum-entropy basis was used to improve compression rate [6]. In Huffman coding scheme, splitting an original symbol sequence into sub-sequences was shown to give a better compression rate on AR1, ECG and seismic signals at several SNR [7]. In [7], the proposed recursive splitting method splits a symbol sequence into subsequences, such that it makes the symbol probabilities different for each subsequence. Thus, individual Huffman coding of each sequence reduces the total number of bits used for the codewords. All those practical efforts demonstrate us that problem of sequence partitioning is a substantial task in a coding method to improve compression rate. In this study, we address the role of the sequence partitioning on the overall compression rate of the data sequences. In this point of view, we theoretically inquire the relation of overall compression rate with the sequence partitioning regardless of coding methodology.

This paper investigates effects of sequence partitioning on the compression rate. Preliminarily, the study demonstrate that one can always found a data partition that makes entropy rate at each subsequence lower than original data sequence even if the information source model is zero-order model. A zero-order information source model is the worst case for coding methods in term of compression performance, since there is not any statistical link between elements of sequence [1]. An assumption of the zero-order statistical model of data source also implies the case that the coder of sequence is ignorant of the nature of the data source. So, the results of this study are not depended of any coding methods. Our investigation focus on the compressibility of partitioned data sequences regardless of coding method. For this proposes, a brief analysis on the overall compression rate of partitioned data sequences is carried out and the factors, affecting overall compression rate, are discussed. A lower bound for the overall compression rate of a partitioned data sequence is derived in the light of Shannon's compression limit. Moreover, an optimization problem, which is independent of coding methods and statistical feature of data, is put aside for future works.

II. Methodology

A. Basic Definitions

Let an finite set of data be $X=\{x_1, x_2....x_r\}$ and a finite set of symbol (Alphabet) be $A=\{s_1, s_2....s_m\}$, where $m>1$. Data set X is composed of elements of the symbol set A. The set A is commonly called as source alphabet. A binary coding function is given as $\phi(.): X \to \{0,1\}$. In such case, a binary coded sequence can be express as $\{\phi(x_1), \phi(x_2), \phi(x_3)..\phi(x_r)\ldots\}$. Compression rate for a set X, coded by $\phi(.)$, can be defined as

$$R = T/l. \quad (1)$$

Here, T is the total number of elements in the binary coded sequence and l is the number of elements in the data set X.

Entropy rate of a data set formed by the m-symbol set A

B. B Alagoz, was with Inonu University, Department of Electrical-Electronics, Malatya, Turkey (e-mail: baykant.alagoz@inonu.edu.tr).
H. Alisoy, was with Inonu University, Department of Electrical-Electronics, Malatya, Turkey (e-mail: halis@inonu.edu.tr).

was given as $H = \log_2 m$, when the data set X was produced by a zero-order source model. A zero-order source model is assumes that there is not any statistical link between elements of data set X [1]. Entropic volume of a data sequence is defined total entropy contained by a data sequence with length l and expressed as lH.

B. Entropy Rates of Partitioned Data Sets

This section is devoted to theoretically show that any data sequence can be partitioned into subsequences such that entropy rate of each sequence is smaller than the entropy rate of original sequence.

Theorem 1:
Any finite data set, given by $X = \{x_1, x_2 .... x_r\}$ and obtained from a zero-order model source, is split into subsets $X_1, X_2, ..., X_g$, where $g \in [2, r]$. Entropy rate of each subset is equal or lower than entropy rate at X.

Proof:
If X is a finite set, the symbol set of X, denoted by A, has to be finite as well. Let the number of elements in a finite set A denoted by m. The entropy rate of X set is written as $H = \log_2 m$. Since any A_i symbol set of the subset X_i is also contained in the set A, the number of elements in any subset A_i will be equal or lower than m. Hence, the entropy rate at a subset X_i, denoted by H_i, will be equal and lower than H as well. So, the property of $H_i \le H$ is valid for any partitioning of a finite data set.

Theorem 2:
Let an infinite set of data be $X_\infty = \{x_1, x_2 .... x_r ...\}$ and suppose that it is generated by a zero-order source. For a symbol set $A = \{s_1, s_2 .... s_m\}$, There is always one partition of X_∞ such that the entropy rate of the each subset is lower than the entropy rate of X_∞.

Proof:
One can always form a subset from the first $m-1$ elements of X_∞. Lets denote this subset by X_1. For a zero-order source model, entropy rate for the set X_∞ can be given as $H = \log_2 m$. For the subset X_1; since it has $m-1$ elements, number of elements in symbol set of X_1 never becomes larger than $m-1$. So, this specifies a upper bounds for entropy rate of X_1 is written as

$$H_1 \le \log_2 (m-1) \qquad (2)$$

Therefore, $H_1 < H = \log_2 m$, one can state that it is possible to find out a subset of X_∞, whose entropy rate is lower than entropy rate of X_∞.

Let the next $m-1$ elements of X_∞ form the subset X_2 and the following $m-1$ elements of X_∞ form the subset X_3 and so on. Thus, X_∞ is partitioned to $X_1, X_2, X_3, \ldots$ subsets, such that, the entropy rate of each subset X_i is lower than the entropy rate at X_∞. So, $X_\infty = X_1 \cup X_2 \cup X_3 \cup .....$ and all $H_i < H$, one can state that "at least one partition of the data set X_∞ can be always found such that the entropy rate at each subset is lower than entropy rate of the set X_∞".

Definition 1(Excessive partitioning):
When the element number of each subsets is less than element number of symbol set A, such a partitioning of data set X is referred to as excessive partitioning. Excessive partitioning always reduces the compression rate due to Theorem 2.

Definition 2(Heuristic partitioning):
When the number of elements of subsets is adjusted intelligently, these partitioning of data set X is called as heuristic partitioning. Heuristic partitioning may reduce the compression rate of data sequence more than excessive partitioning if generated by non-zero order source models.

Definition 3(Constant length partitioning):
If the number of elements of each subset is equal, this partitioned is referred to constant length partitioning.

Definition 4 (Variable length partitioning):
If the number of elements of subsets is not equal, this partitioning is referred to as variable length partitioning.

Definition 5 (Entropic partitioning):
If a partition of a sequence decreases the overall compression rate of a sequence, this partitioning is called entropic partition. Entropic partition set covers excessive partitioning, heuristic partitioning, constant length partitioning, variable length partitioning if anyone reduces the compression rate of sequences.

Theorem 1 and 2 clearly reveals that the partitioning of a data set can provide a reduction in entropy rate of a data streams regardless of statistical characteristic of the data sequences. For instance, excessive partitioning always reduces entropy ($H_i < H$). However, heuristic partitioning strategies may reduce compression rate more than excessive partitioning. So, we need to figure out overall compression rate of a partitioned data sequence in order to make a direct assessment about impacts of sequence partitioning on the overall compression rate of digital data sequences. In the flowing section, overall compression rate of partitioned sequences are inspected.

C. Overall Compression Rate in a Partitioned Data Sequence

This section is devoted to analyze overall compression rate of partitioned finite data sequences. Firstly, lets figure out the overall compression rate of a finite data sequence D, in the case that it is split into k number of subsequences, denote by

d_i, $i \in [1,k]$. The number of elements in each subsequences d_i is denoted by a_i. Secondly, let assume the binary coding function family denoted by $\phi^j(.)$ used in coding of these subsequences. Assuming that the best binary coding function providing the lowest compression rate for a subsequence is chosen from the $\phi^j(.)$, the overall compression rate of D in this partitioning can be expressed as,

$$R = \sum_{i=1}^{k} w(a_i) \cdot R_i^* , \quad (3)$$

where R_i^* is the compression rate, obtained in the coding of subsequent d_i by mean of the best binary coding function. The term $w(a_i)$ is the size weight of subsequence d_i in the sequence D and expressed as $w(a_i) = a_i / l$. Here, l is total number of elements in the sequence D. (See the appendix for the derivation of Equation (3)) The R_i^* is considered to include an additional bit rate ε_i, which is reserved for the redundant coding. The redundant coding mainly resides in headers of data packs.

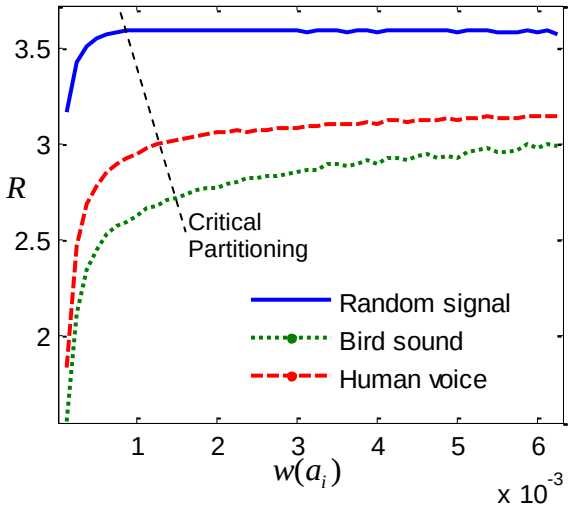

Fig.1. Overall compression rate calculated for equal sized partitioning of data sequences (Random signal, Bird sound and Human voice). Compression rate of pseudo coding function for each subsequences is assumed to $R_i^* = \beta \cdot H_i + \alpha \cdot H_i$.

Example 1:
Fig. 1 illustrates overall compression rates calculated for an constant length partitioning of various time series signals ($a_1 = a_2 = ... = a_k$ and $w(a_1) = w(a_2) = ... = w(a_1) = a_i / l$) in the case of a pseudo coding function, of which the compression rate is assumed as $R_i^* = \beta \cdot H_i + \alpha \cdot H_i$. Here, parameter $\beta > 1$ is used to conform the condition of $R_i^* > H_i$ due to Shannon's limit of lossless compression. We assume to be $\beta = 1.1$ for our pseudo coding scheme. The parameter $\alpha = 0.1$ is stands for the redundant code rates allocated for header to send symbol set and other required codes. The entropy of each subsequent is calculated $H_i = \log_2 m_i$ where m_i is the number of symbol in the subsequence i. In the figure, a critical partitioning line, where compression rate began to decreasing sharply, is shown in overall compression rate plots of time series signals. Bird sound and human voice contains data set generated by a none-order source model. Since there is statistical links between elements, the partitioning and compression rate can decrease for larger subsets compared to random signal set. The random signal is supposed to simulate a none-order source model.

Since $R_i^* > H_i$ according to Shannon's limit of lossless compression [1-2], a lower bound for the overall compression rate can be written as,

$$R > \sum_{i=1}^{k} w(a_i) \cdot H_i . \quad (4)$$

In order to point out effects of sequence partitioning on the compression rate, it will be convenient to express the deviation in the compression rate after a partitioning, which is defined as $\Delta R = R' - R$. Here, R' represents the compression rate in the coding of original sequence without a partitioning and it also satisfies the condition of $R' > H$ due to Shannon's limit. After a sequence partitioning, the deviation in the overall compression rate can be written as: (See the appendix for the derivation of Equation (5)).

$$\Delta R > \sum_{i=1}^{k} w(a_i) \cdot (H - H_i) . \quad (5)$$

If the condition of $H_i \le H$ from Theorem 2 and $w(a_i) \in (0,1]$ is considered, after partitioning sequence, the deviation in compression rate is found as $\Delta R \ge 0$. This noteworthy finding suggests that a partitioning, independently from coding functions and in the absence of a prior statistical knowledge, can reduce the compression rate. In the case that the redundant coding used in headers of data packs are taken into account, the condition of $\Delta R \ge \varepsilon$ should be met to have a better compression after a partitioning. Here, ε represents additional bit rate caused from redundant codes used in applications. In practice, ε is mainly negligible compared to values of R.
Considering Equations (3) and (4), the following substantial remarks can be listed:

i) Overall compression rate of a partitioned sequence strongly depends on the compression rate of each subsequence and their sizes. In fact, the overall compression rate in a partition is a size-weighted average of compression rates of all subsequences. In order to reach a lower overall compression, one should establish an optimal partition strategy such that the subsequences exhibiting a lower compression rates are the larger in size.

ii) It is not a necessity to use one type coding scheme for the coding of all subsequences. The one providing a lowest rate of compression from the coding scheme family can be selected to

code a subsequence and others can be used for other sequence to have a better overall compression rates. So, multi-coding approach can be more effective to improve compression rates.

iii) In order to enhance overall compression rate, the sequence partitioning has to comply with the condition of $\Delta R \geq \varepsilon$.

III. A Discussion on Overall Compression Rate for Optimal Partitioning of Data Sequence

Let assume that a finite length sequence X with entropy rate H is split in subsequence x_i with length of $a_1, a_2, ..., a_k$ and entropy rate H_i. Total entropic volume of X can be defined as, $H\sum_{i=1}^{k} a_i$ and overall entropic volume of partitioned X sequence can be expressed as $\sum_{i=1}^{k} a_i H_i$. Due to partitioning, reduction rate in entropic volume can be written as, $(\sum_{i=1}^{k} a_i H_i) / H\sum_{i=1}^{k} a_i$. In order to improve compression rate of a data sequence by entropic partitioning, the reduction rate in entropic volume should be decreased.

To have better compression rate, the following partitioning rules for entropic partitioning, can be listed:

i) For the data segments having higher entropy rates, form subsequences with a shorter length,

ii) For the data segments having lower entropy rates, form subsequences with a larger length.

iii) Due to Shannon's limit of lossless compression ($R_i > H_i$ and $R > H$), coding method used to compress data is a important factor for the success of compression. That is why, entropic partitioning should be performed by considering coding methods.

Example 2:

A visual example for entropic partitioning strategy is illustrated in Fig. 2. In the figure, original sequence, represented by a large dash rectangle, has the length of $\sum_{i=1}^{5} a_i$ and the overall entropy rate, $H = H_1$. Subsequences are represented by the rectangular areas in different color tones. They have the sizes of a_i and their entropy rates denoted by H_i. In this visual partitioning example, by using Equation (5), the deviation in overall compression rate of original sequence can be expressed as $\Delta R > w(a_2)(H_1 - H_2) + w(a_3)(H_1 - H_3) + w(a_5)(H_1 - H_5) > 0$. This result verifies that a reduction in overall compression rate can be possible by this partitioning. The gray zone with scan lines represents reduced entropic volume as a result of entropic partitioning of original sequence.

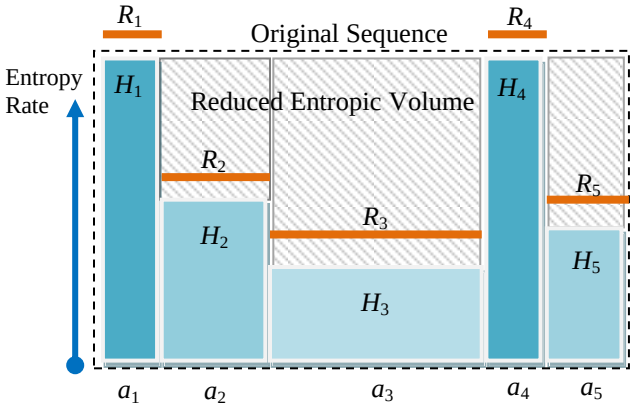

Fig.2. An example of good partitioning reducing entropic volume of original sequence

Entropic partitioning is not dependent of coding methods. A problem of a good entropic partitioning that aims to reduce overall compression rate can be defined as,

$$\Delta R_{opt} = \max_{a_i} \{\sum_{i=1}^{k} w(a_i) \cdot (H - H_i)\}. \quad (6)$$

In the case of a predetermined set of coding schemes, the problem of an optimal partitioning is argued in detail, below:
An optimal partitioning of data sequence can be defined as a partitioning that makes the overall compression rate globally minimum, and it can be simply expressed as

$$R_{opt} = \min_{a_i, R_i} \{\sum_{i=1}^{k} w(a_i) \cdot R_i^*\}. \quad (7)$$

For the practical point of view, the problem of finding an optimal partitioning for a data sequence turns into the problem of finding a_i, R_i^* parameters such that they yields a minimal overall compression rate. An objective function to be optimized can be fashionably written as,

$$E = \sum_{i=1}^{k} (w(a_i) \cdot R_i^*)^2. \quad (8)$$

Overall compression rates obtained for a constant length partitioning (without optimization) and a variable length partitioning (with optimization in accordance with the Equation (8)) is compared in Fig. 3. In this straightforward optimization method, an original data sequence first splits into equal sized subsequences, which is also the case of "without optimization", then, each subsequences shrink or expand toward its neighbors in order to minimize the objective function E given by Equation (8). The figure reveals that variable length partitioning by optimization further decreases compression rate of non-zero order source models.

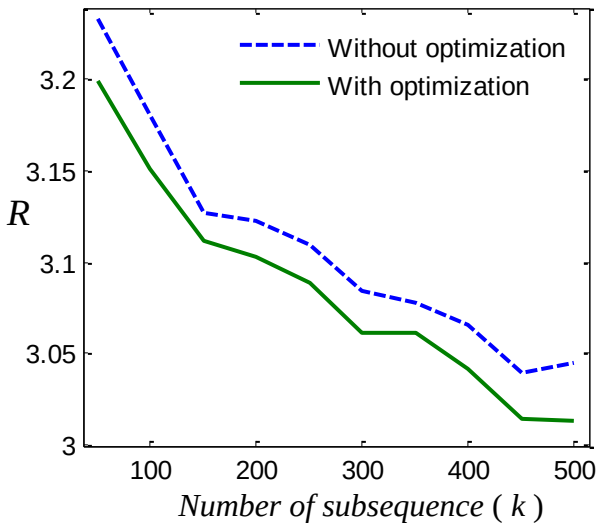

Fig. 3. Overall compression rates calculated for the both case of an equal sized partitioning (without optimization) and a variable size partitioning(with optimization) of data sequences from human voice. Compression rate of the pseudo coding function is assumed as $R_i^* = \beta \cdot H_i + \alpha \cdot H_i$ for $\beta = 1.1$ and $\alpha = 0.1$.

For a faster approximation to the optimal solution for entropic partitioning, a partitioning can be performed subject to a constant bit-length constraint, which is arithmetically defined as,

$$C = a_i \cdot R_i^* , \tag{9}$$

where $C \in R$ is a constant that specify a target length for subsequences in term of bits. A new version of the objective function for an optimal partitioning with a constant bit-length of subsequences can be written as,

$$E = \sum_{i=1}^{k} [(w(a_i) \cdot R_i^*)^2 + (C - a_i \cdot R_i^*)^2] . \tag{10}$$

The solution of this optimization problem was not a preference of this work. We aim to show existence of an optimization problem for a good partitioning, which is applicable in all practical coding schemes in the absence of a prior knowledge about statistical nature of data sequence.

IV. Conclusions

The entropy rate at a data sequence can be simply decreased by splitting it. This enables compression of data sequence regardless of the coding scheme. The property of $\Delta R \geq \varepsilon$ in a partitioning ensures us that the data sequence partitioning decreases the overall compression rate, however, the amount of reduction in the overall compression rate depends on two terms; compression rate of coding methods (R_i^*) and the ratio of subsequences size to original sequence size ($w(a_i) = a_i / l$). In the paper, a theoretical discussion for a general optimal partition strategy, which is applicable to all coding techniques, was given and a corresponding optimization problem to improve overall compression rate is defined. We see that it will be possible to utilize a collaboration of various coding methods in a sequence partitioning problem to reach a better compression performance and referred it as to multi-coding optimal partitioning.

The findings of this theoretical work contribute to comprehension of roles of partitioning in data compression. Bounds of overall compression rates for partitioned sequences is analytically derived (Equation (4)), which can, indeed, be considered as an extension of Shannon's limit of lossless compression rate for the case of sequences splitting. Specifically, for the case of $k = 1$, it yields Shannon's limit for lossless compression.

With a reverse consideration, one can also state that combining data packs with different entropy rates in order to obtain a larger data set can increase overall entropy due to the some waste of entropic volume. Entropy rate of combined data set is determined by the largest entropy rate of data packs.

Appendix

Derivation of Equation (3):

A finite sequence with l elements splits into k number of subsequences. Each subsequence has the lengths of a_i and the compression rate of R_i^*. R_i^* is the best compression of sequence defined as $R_i^* = \min\{R_i^j\}$ for a binary coding function family $\phi^j(.)$. R_i^j is the compression rate in the coding of the subsequence i by $\phi^j(.)$. The total bit numbers used in coding all subsequences by using the best $\phi^j(.)$s from the coding function family can be written as,

$$T = \sum_{i=1}^{k} a_i \cdot R_i^* .$$

Compression rate was defined as $R = T / l$. So, the overall compression rate for a partitioned sequence by using the best coding functions can be written as,

$$R = \sum_{i=1}^{k} \frac{a_i}{l} \cdot R_i^* .$$

When $w(a_i) = a_i / l$ is considered, one obtains the overall compression rate as:

$$R = \sum_{i=1}^{k} w(a_i) \cdot R_i^* .$$

Derivation of Equation (5):

In the coding of a sequence without partitioning, compression rate can be written as $R' > H$ due to Shannon's limit. With using Equation (4) and $R' > H$, the deviation in compression rate, which is $\Delta R = R' - R$, can be written as

$$\Delta R > H - \sum_{i=1}^{k} w(a_i) \cdot H_i .$$

Here, $w(a_i) = a_i / l$ and $l = \sum_{i=1}^{k} a_i$ for a k number partitioning. In this case,

$$\Delta R > H - \sum_{i=1}^{k} w(a_i) \cdot H_i = \frac{\sum_{i=1}^{k} a_i}{l} H - \sum_{i=1}^{k} \frac{a_i}{l} \cdot H_i \,,$$

$$= \sum_{i=1}^{k} \frac{a_i}{l} \cdot H - \sum_{i=1}^{k} \frac{a_i}{l} \cdot H_i = \sum_{i=1}^{k} w(a_i) \cdot (H - H_i) \,.$$

Finally, the Equation (5) is obtained as,

$$\Delta R > \sum_{i=1}^{k} w(a_i) \cdot (H - H_i) \,.$$

REFERENCES

[1] C.E. Shannon and Weaver W., *The Mathematical Theory of Communication*, Illinois, 1949.

[2] T.M. Cover and J.A. Thomas, Elements of Information Theory, Wiley India Pvt Ltd., 1991.

[3] D.A. Huffman, "A Method for the Construction of Minimum Redundancy Codes", Proceedings of the IRE, 40, 1952, pp. 1098-1101.

[4] J. Ziv and A. Lempel, "A Universal Algorithm for Sequential Data Compression", IEEE Transactions on Information Theory, 23, 1977, pp. 337-342.

[5] J. Ziv and A. Lempel, "Compression of Individual Sequences Via Variable-Rate Coding", IEEE Transactions on Information Theory, 24, 1978, pp. 530--536.

[6] R.R. Coifman, M.V. Wickerhauser, "Entropy-Based Algorithms for Best Basis Selection", IEEE Transactions on Information Theory, 38, 1992, pp.713-718.

[7] K. Skretting, J.H. Husoy, S.O. Aase , "Improved Huffman coding using recursive splitting", Norwegian Signal Processing Society Conference (NORSIG-99),Norway, 1999.

[8] T.A. Welch, "A Technique for High-Performance Data Compression", Computer, 1984, pp. 8-18,.

[9] R.M. Hassan and B. Nath, "Data Compression Using Huffman Coding A Novel Approach", International Conference on Applied Computing (IADIS-2005), Portugal,2005.

[10] T. Bonny, J. Henkel, "Instruction Splitting for Efficient Code Compression", Design Automation Conference, 2007. DAC '07. 44th ACM/IEEE, 2007, pp. 646-651.

BIOGRAPHIES

Baris Baykant Alagoz was graduated from University of Istanbul Technical University department of Electronics and Communication Engineering in 1998. He worked for Alcatel Microelectronics and Turkish Telecom several years. He is following PhD at Inonu University of Department of Electrical &Electronics Engineering.

Hafiz Z. Alisoy was graduated from Moscow Technical University department of Electro-Physics Engineering in 1982. He had his PhD degree from USSR Science Academy Physics Institute of P.N. Lebedyev and Doctor of Sciences degree (DSc) from International Ecology-Energy Academy. He became as Full Professor in 1995. He received award of Young Scientist. He works at Inonu University department of Electrical &Electronics Engineering.

Fault Detection Considerations in Silicon Based MEMS Resonators by Observing Changes in Dynamic Behaviour

S. İkizoğlu and M. Akyol

***Abstract*- This study is about fault detection in silicon-based MEMS resonators. The main idea in finding out the failure is to establish a proper relationship between the mechanical structure and its electrical equivalent and prosecuting related measurements. In order to determine the type of defect, the electrical equivalent circuit is referenced considering the parasitic effects. Among various possible faults cracks in the beam and particle adhesion are selected to verify the validity of the approach. Simulations are carried out to study the effect of defects on the resonance frequency and amplitude. Results coincide greatly with those of similar investigations giving motivation for further studies to penetrate deep into the matter, thus not being restricted with defining the trouble, but even locate the failure.**

***Index Terms*- MEMS Resonator, resonance frequency, quality factor, transduction factor**

I. INTRODUCTION

DAY by day the application of MEMS devices is growing up rapidly in various areas due to their superior advantages such as low power consumption, small size, long life and low cost [1]. Among numerous application areas MEMS resonators find also remarkable place [2-4]. This is because the MEMS resonators offer excellent properties than their IC-counterparts with their long-term stability and extremely high quality factor [5]. Thus, they are widely used in oscillators and filters.

On the other side, with the increasing demand toward MEMS devices, the requirement for reliability is also ascending rapidly. Concerning this issue, several precautions are taken and measurements are carried out during the fabrication process. Additionally, observations are made in dynamic conditions. Investigations put forward that there are several reasons which cause malfunction of MEMS resonators. Among all, faults caused by particle adhesion and cracks are at the top of the list [6]. Besides these, friction due to particle contaminants, fatigue of the material, deformation, etching faults etc. also lead to failure. Several studies have been carried out to describe the relationship between the defect and the corresponding parameter [7-10].

S. İkizoğlu is with the Department of Control and Automation Engineering, Istanbul Technical University, Istanbul, Turkey (e-mail: ikizoglus@itu.edu.tr).

M. Akyol is with Turkish Airlines Technique Inc., Turkey.

In this paper we will mainly focus on faults caused by cracks and particle adhesion, but the way we define the source of the trouble is also valid to find out of others. Any defect in the structure leads to changes in the natural frequency of the MEMS resonator, in the amplitude of the vibration or in the value of the quality factor. Thus, representing the electrical circuit with its y-parameters will be helpful for the analysis. The parameter y_{21} relates the output current to the input voltage giving the highest value at the resonance frequency.

II. MEMS RESONATOR MODEL

There are various structures for MEMS resonators. While the comb structure is becoming popular in recent years, micro-flap and bridge resonators are also used in different applications [11]. Since for all structures we speak of 'distributed' mass and elasticity, MEMS resonators are investigated using the 'lumped' mass-spring or electrical-equivalent model. The mass-spring model (Fig. 1a) has its well- known equation as

$$m\ddot{x} + \gamma\dot{x} + kx = F \tag{1}$$

where m represents the effective mass and γ and k stand for damping constant and effective spring constant, respectively; F is the external force acting on the system. Here,

$$k = \omega_0^2 m \tag{2}$$

where ω_0 is the first natural frequency of the resonator beam. The mass-spring model can be related to the electrical model (Fig.1b) with following equivalencies:

$$\dot{x} = i\ ,\ \gamma = R\ ,\ m = L\ ,\ k = 1/C\ ,\ F = u$$

where u is the voltage applied, and i is the current through the series circuit.

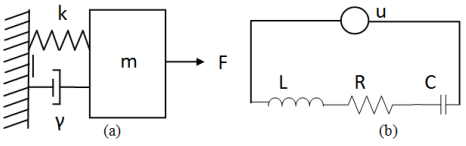

Fig.1. a) Mass-spring model b) Electrical equivalent

In MEMS resonators, first the excitation voltage is converted into mechanical vibration which is further converted into current i defined in the electrical equivalent circuit. This capacitive transduction can be formulated as follows:

$U=U_{DC}+U_{AC}$ is applied to the resonator, where U_{DC} serves for two the purposes: The one is that the resonator does not oscillate at twice the fundamental resonance frequency [12]. It further is directly effective on the transduction. The capacitance C_0 of the capacitor that is formed by the base electrode and the beam changes due to the excitation voltage U as

$$C = \varepsilon \frac{A}{d-x} = C_0 \frac{d}{d-x} \quad (3)$$

with $C_0=\varepsilon A/d$, where A is the effective area, ε the dielectric constant, d the plate separation and x the change in d due to exerted electrostatic force. Thus, the energy of the capacitor is $W = CU^2/2$ and the force acting onto the beam is given as

$$F = \frac{\partial W}{\partial x} = \frac{1}{2}\frac{\varepsilon A}{(d-x)^2}U^2 \quad (4)$$

Assuming x<<d, the AC component of this force can be approximately calculated as

$$F_{AC} = \frac{U_{DC}U_{AC}C_0}{d} = \eta U_{AC} \quad (5)$$

Here,

$$\eta = U_{DC}C_0/d \quad (6)$$

is called the transduction factor. Since the current is defined as $i=\partial Q/\partial t$ (Q: charge) and for a capacitor $C=\partial Q/\partial U$, the current through the resonator can be expressed as

$$i = \frac{\partial(CU)}{\partial t} = U\frac{\partial C}{\partial t} + C\frac{\partial U}{\partial t} \approx \eta\frac{\partial x}{\partial t} + C_0\frac{\partial U_{AC}}{\partial t} \quad (7)$$

Consequently the electrical equivalent circuit of the resonator can be drawn as in Fig.2.

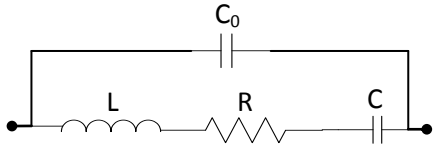

Fig.2. Electrical equivalent circuit of a MEMS resonator

In Fig.2 following equivalencies are valid [13]:

$$L = \frac{m_{eff}}{\eta^2}, C = \frac{\eta^2}{k_{eff}}, R = \frac{\sqrt{k_{eff}m_{eff}}}{Q\eta^2} \quad (8)$$

Here m_{eff} and k_{eff} stand for effective mass and effective stiffness of the resonator, respectively; $Q \approx m\omega_0/\gamma$ represents the quality factor. At this point it is worth to note that the effective spring constant has two main components and is given as

$$k_{eff} = k_i - k_s \quad (9)$$

where k_i is the initial spring constant and k_s represents the softening effect given by

$$k_s \approx \frac{\varepsilon_0 A_{eff} U_{DC}^2}{d^3} \quad (10)$$

with A_{eff} being the exposed area of the beam and d the plate separation [13].

III. MODEL INCLUDING PARASITIC EFFECTS

A. Resonator Model

The common used model of a MEMS resonator is as in Fig.2. Fig.3 shows the cross section of a micro-flap resonator [14]. Here, C_{p1} and C_{p2} represent shunt capacitances of field oxide between the electrodes and the substrate. Thus, Tanaka et al suggest that according to Fig.3 the electrical equivalent circuit of a resonator should be constructed as in Fig.4 which takes the parasitic effects into consideration [14]. Here, C_{pad} represents the shunt capacitance between Si-substrate and the measurement pad and $\frac{1}{C_p} = \frac{1}{C_{p1}} + \frac{1}{C_{p2}}$.

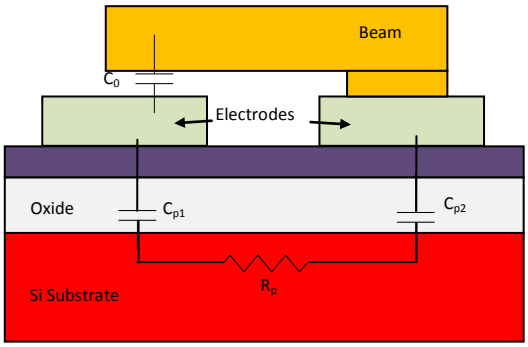

Fig.3. Cross section of a micro-flap resonator.

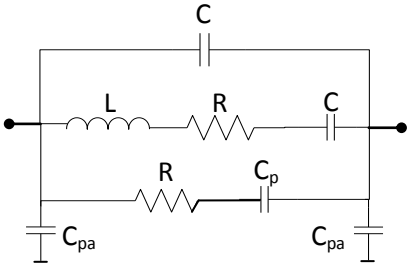

Fig.4. Equivalent circuit of the MEMS resonator considering parasitic effects.

B. y-parameter Equivalent Circuit

For the equivalent circuit in Fig.4 it is obvious that at the resonance frequency of the resonator, y_{12} ($=y_{21}$) parameter will have its highest value. For this circuit the expression for y_{12} can be derived as follows:

$$y_{12} = \frac{As^4+Bs^3+Ds^2+Es}{Fs^3+Gs^2+Hs+1} \quad (11)$$

where

A= $R_pC_0C_pLC$
B= $R_pC_0C_pRC+C_0LC+ C_pLC$
D= $CC_pR_s+C_0R_pC_p+ C_0RC+ CC_pR_p$
E= C_0+C+C_p
F= R_pC_pLC
G= $R_pR_sC_pC+CL$
H= C_pR_p+RC

IV. EFFECT OF FAULTS ON CHARACTERISTIC CURVES

In order to examine the effect of the changes in several parameter values on the resonance frequency, a set of initial values are taken as reference with:

C_0=25e-15F;
C_p=20e-15F;
C_{pad}=0.8e-12F;
C=1e-15F;
R=100e3Ω;
L=100e-3H;
R_p=0.01Ω.

These values give a resonance frequency of f_0=15.883MHz, while this frequency would be 15.915MHz for the equivalent circuit in Fig.2.

Below is investigated how several deviations from the initial values would affect f_0.

Change in transductance η: The relative sensitivity of L toward η is $\partial L/\partial\eta/L = -2/\eta$. Thus, a change of 1% in η results in a change of -2% in L. On the other side, a change in η ($\Delta\eta$) leads to a change in C as $\Delta C/C=2\Delta\eta/\eta$, thus cancelling the effect of the change in L for the resonance frequency, if the equivalent circuit is taken as in Fig.2. But this will not be case, if the change in η is due to a change in the polarization voltage U_{DC}, because U_{DC} is also effective in k_s. Considering the equivalent circuit as in Fig.2, the resonance frequency is calculated as,

$$\omega_0 = \frac{1}{\sqrt{LC}} = \sqrt{\frac{k_{eff}}{m_{eff}}} = \sqrt{\frac{k_i}{m_{eff}}\left(1-\frac{k_s}{k_i}\right)} \quad (12)$$

As R is also dependent on k_{eff}, not only the resonance frequency, but also the amplitude of the curve will be affected. Fig.5 shows the dependency of the resonance frequency on U_{DC} with the assumption that for the initial case U_{DC}=10V.

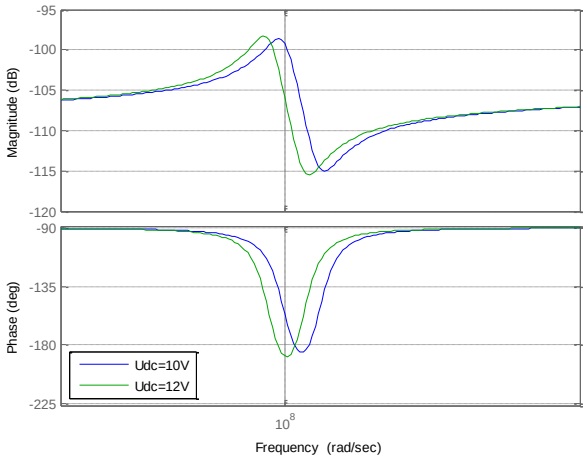

Fig.5. Effect of the polarization voltage upon the resonance frequency and amplitude

Change in effective stiffness: A crack in the beam will decrease its stiffness. If we assume that the effective mass is being kept constant, the decrease in stiffness increases C and reduces R according to Equations in (8). The result is demonstrated in Fig.6.

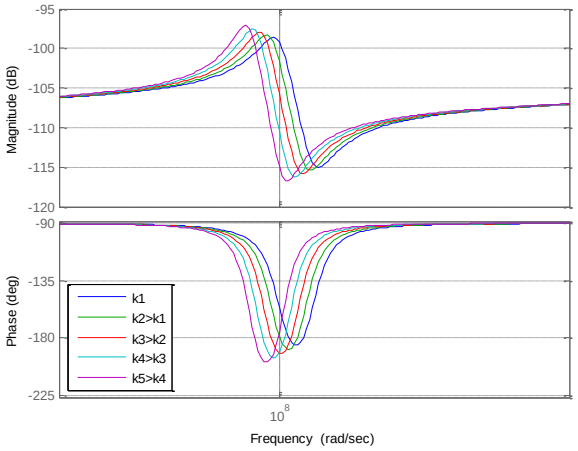

Fig.6. Effect of the effective stiffness k upon the resonance frequency due to a beam crack.

If a particle adhesion fault exists, the effective stiffness will increase and accordingly an increase in frequency eventuates. This condition is illustrated in Fig.7. We clearly observe that besides the increase in frequency, the amplitude decreases, thus reducing the sensitivity.

A particle adhesion will also decrease C_0 since it effects the separation *d* between the base and the beam. The change of the frequency characteristic only due to C_0 is illustrated in Fig.8. It is observed that besides a slight shift in the resonance frequency, mainly the overall amplitude decreases with decreasing C_0.

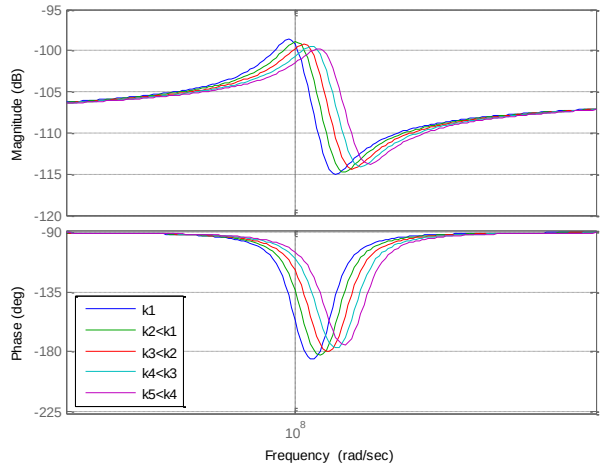

Fig.7. Effect of the effective stiffness k upon the resonance frequency due to particle adhesion fault.

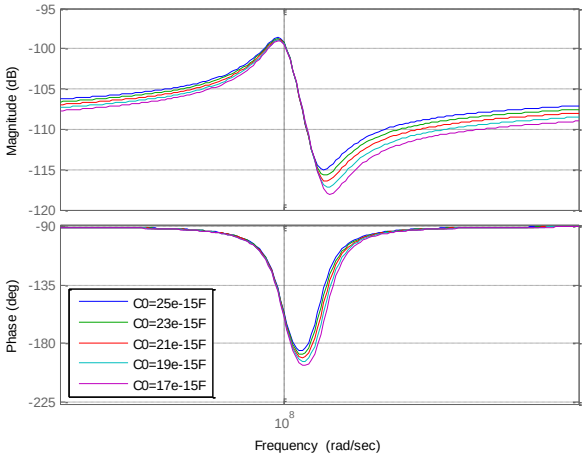

Fig. 8. Effect of C_0 on the frequency characteristic of the resonator.

V. CONCLUSION AND FUTURE WORK

In this study fault detection approach for silicon based MEMS resonators is handled. For this purpose, an electrical equivalent circuit is related to the mechanical spring-mass model of the resonator, where parasitic effects are also taken into account. The main idea is based upon the fact that any defect in the structure leads to a certain shift of the resonance frequency and change in the amplitude and quality factor. Mainly the effect of two defects -crack in the beam and particle adhesion fault- is analyzed. The results coincide greatly with those of other studies [6,15,16]. This is considered as a proof of the validity of the approach and encourages for extending the studies to cover other possible faults. The next step will be to define more precisely the relationship between the structural troubles and related changes in the electrical equivalent circuit. It is clear that a fault may influence several parameters. On the other side different defects may be effective on the same parameter in different proportions. Hence, a detailed investigation with experimental approval is needed in order to concretize the fault.

This study has mainly fucused on the way how to approach to find out the reason of the malfunction of a MEMS resonator. On this way several assumptions have been made such that the nonlinearities of the spring constant in the mechanical equivalent structure have been disregarded. Future work will cover the deep study taking as many effective parameters into consideration as possible. A major part of future work should also be constituted by the interrelation between the location of the defect and the corresponding deviation in functioning of the resonator.

REFERENCES

[1] S. D. Senturia, "Microsystem Design", *Kluwer Academic Publishers*, 2nd ed., Massachusetts, 2001.

[2] T. Clark, C. Nguyen, L. P. B. Katehı, G. M. Rebeız, "Micromachined devices for wireless communications", *Proc. of the IEEE*, vol. 86, no. 8, pp 1756-1768, Aug. 1998.

[3] W.T. Hsui, T. Clark, C. Nguyen, "Stıffness-compensated temperature-ınsensıtıve mıcromechanıcal resonators", *Proc. of the IEEE*, pp. 731-734, 2002.

[4] N. Sepulveda, D. Aslam, J.P. Sullivan, "Polycrystalline diamond MEMS resonator technology for sensor applications", *Diamond & Related Materials, Elsevier*, vol. 15, pp 398 – 403, 2006.

[5] V. Kaajakari, "Theory and analysis of MEMS resonators", *VTI Technologies*, 2011.

[6] A. Izadian and P. Famouri, "Fault diagnosis of MEMS lateral comb resonators using multiple-model adaptive estimators", *IEEE Transactions on Control Systems Technology*, vol. 18, no. 5, pp. 1233-1240, Sept. 2010.

[7] N. Deb and R. D. Blanton, "High-level fault modeling in surface-micromachined MEMS" *Design, Test, Integration, and Packaging of MEMS/MOEMS, Proceedings of SPIE*, vol. 4019, pp. 228–235, May 2000.

[8] R. Reichenbach, R. Rosing, A. Richardson, and A. Dorey, "Finite element analysis to support component level fault modelling for MEMS," *Design, Test, Integration, and Packaging of MEMS/MOEMS, Proceedings of SPIE*, vol. 4408, pp. 147–158, April 2001.

[9] Z. Chen, Y. Y. He, F. L. Chu, and J. Huang, "Dynamic characteristic analysis of the micro-structure with defects," *Chinese Journal of Mechanical Engineering*, vol. 40, no. 6, pp. 23–27, 2004.

[10] S. Mir, B. Charlot, and B. Courtois, "Extending fault-based testing to microelectromechanical systems," *Journal of Electronic Testing: Theory and Applications*, vol. 16, no. 3, pp. 279–288, 2000.

[11] D. Paci, M. Mastrangeli, A. Nannini, F. Pieri, "Modeling and characterization of three kinds of MEMS resonators fabricated with a thick polysilicon technology", *Analog Integr. Circ. Sig. Process.*, vol. 48, pp. 41–47, 2006.

[12] M. W. Putty, S. C. Chang, R. T. Howe, A. L. Robinson, K. D. Wise, "One-port active polysilicon resonant microstructures", *Proc.IEEE Micro Electromechanical Systems*, pp.60-65, Feb.1989.

[13] S. Chowdhury, M. Ahmadi, W. C. Miller, "Pull-in voltage calculations for MEMS sensors with cantilevered beams", *IEEE-NEWCAS the 3rd International Conference*, Québec City, Canada, vol. 19-22, pp.143 – 146, June 2005.

[14] K. Tanaka, R. Kihara, A. S. Amores, J. Montserrat, "Parasitic effect on silicon MEMS resonator model parameters", *Proceedings of the IEICE General Conference*, 2001.

[15] B. Chariot, S. Moussouris, S. Mir and B. Courtois, "Fault modeling of electrostatic comb-drives for MEMS", *Symposium on Design. Test, and Microfabrication of MEMS and MOEMS, SPIE* vol. 3680, Paris, France, 1999.

[16] S. A. Rittenhouse, "Diagnosis of Operational Changes in Microelectromechanical Systems via Fault Detection", *Thesis submitted to the College of Engineering and Mineral Resources at West Virginya University*, 2004.

Serhat Ikizoğlu was born in Istanbul/Turkey in 1957. He received his BSc Degree from Istanbul Technical University (ITU), Electronics and Communication Engineering Department in 1980. He graduated from the same university, Control and Computer Engineering Department with MSc and PhD Degrees in 1982 and 1992 respectively.
He is currently Assistant Professor in Control and Automation Engineering Department at ITU. His research interests are electrical measurement and instrumentation, mechatronics and biomedical engineering.

Muhammed Akyol received his BSc Degree from the Electronics and Telecommunication Engineering at Istanbul Technical University in 2004. He graduated from Electrical Engineering Department in Sept. 2008. He worked at Turkish Airlines Technique Inc. for 4 years.
He is currently a pilot at Turkish Airlines.

Dynamic Stability Improvement of a Power System Based on a PSO-Tuned H_2 Controller

M. Mohseni Mirabadi, N. R. Abjadi, S. Hoghoughi-Isfahani, and S. Shojaeian

***Abstract*—To supply power demands reliably, power system should cope with various disturbances and faults and its stability should be retained. A power system may be failed due insufficient damping of synchronizing torque. In this paper, to improve the dynamic stability of a power system a feedback control based on H2 method is designed. To formulate the problem appropriately, linear matrix inequality (LMI) theory is employed. To optimize the overall closed-loop system response, the parameters of controller is optimized using particle swarm optimization (PSO) algorithm. Simulation results represent the effectiveness and validity of the proposed controller and its superiority over conventional power system stabilizer (PSS).**

***Index Terms*—**Dynamic Stability, Robust Control, Linear Matrix Inequality (LMI), Single Machine Infinite Bus (SMIB), Power System Stabilizer (PSS), H_2Control.

I. INTRODUCTION

WITH the growth of power networks, low frequency oscillations appear in power system. Small and sudden disturbances cause such oscillations. In more cases, these oscillations are damped quickly and the amplitude of the oscillation is under a certain value; but depending on the operating point conditions and system parameters values, these oscillations may become continuing for a long time and in the worst case, their amplitudes are increased. The dynamic stability of the power system is an important factor in development power networks. In [1], using fuzzy logic laws, a controller is designed for STATCOM and the improvement of power system dynamic stability is studied. In [2], a robust controller is proposed for SVC control to improve the damping of synchronous machine oscillations. The achieved results in this work are compared to the ones from a conventional power system stabilizer (PSS). In [3], to increase the dynamic stability a UPFC is employed and two control methods are proposed. In this work the effect of UPFC capacitance value on dynamic stability is investigated. There are various PSS structures; but conventional PSS is still interesting because of its simple structure and good flexibility and feasibility. However the performance of conventional PSS is sensitive to operating point of the system which is changed by load variation; thus the conventional PSS may be failed capability [4]. In [5], the effect of the injected reactive power of STATCOM on grid voltage and the damping of synchronous machine oscillations is investigated. Most of the controllers proposed for this purpose need a perfect model of the power system with good precision. It is worthwhile to note the power system is a nonlinear coupled system. Most of the models used in controller design are a linear approximation around the operating point. Usually the design of the controller is based on the worst operating point and simply the damping torque is increased. With a change in load or system parameters, the good performance of the system is not guaranteed. In this paper, a robust H2 state feedback control to improve dynamic stability of power system in the presence of parametric uncertainties is introduced. This controller overcomes the mentioned difficultly in power system. To achieve the best controller tuning, the particle swarm optimization (PSO) is employed. The obtained results are compared to the results with a conventional PSS.

M. Mohseni-Mirabadi, N.R. Abjadi and S. Hoghoughi-Esfahani are with the Deparetment of Engineering, Shahrekord University, Shahrekord, Iran. (e-mail: Mohsenimehdi.sku@gmail.com, navidabjadi@yahoo.com, said_hoghoughi@yahoo.com)

S. Shojaeian is with the Department of Electrical Engineering, Khomeinishahr Branch, Islamic Azad University, Isfahan, Iran (e-mail: shojaeian@iaukhsh.ac.ir)

II. SELECTED POWER SYSTEM AND IT'S MODELING

The power system under study in this paper is presented in Fig. 1. In this figure, V_t and V_o are terminal voltage and infinite bus voltage respectively. A local load with Y=G+jB admittance is on generator bus and the transmission line is presented with Z=R+jX total impedance [6].

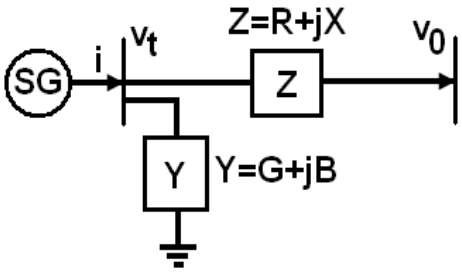

Fig. 1. Selected power system

Considering Heffron-Philips model for a synchronous generator, the model of the system is given by the following equations:

$$\dot{\delta} = \omega_0 \omega \tag{1}$$

$$\dot{\omega} = \frac{1}{M}(T_m - T_e - D\omega) \quad (2)$$

$$\dot{E}'_q = \frac{1}{T'_{d0}}(E_{fd} - E'_q - (X_d - X'_d)i_d) \quad (3)$$

$$T_e = C_3 E'_q \sin\delta + C_4 \sin 2\delta \quad (4)$$

$$i_d = \frac{E'_q - V_o \cos\delta}{X'_d} \quad (5)$$

$$C_3 = \frac{V_o}{X'_d} \quad (6)$$

$$C_4 = \frac{V_o^2}{2}\left(\frac{1}{X_q} - \frac{1}{X'_d}\right) \quad (7)$$

After linearization, considering state variables as $X_1 = \delta$, $X_2 = \omega$, $X_3 = E'_q$ and input variables as $u_1 = E_{fd}$ and $u_2 = T_m$ these equations can be written as:

$$\Delta\dot{X}_1 = \omega_0 \Delta X_2 \quad (8)$$

$$\Delta\dot{X}_2 = \frac{1}{M}(\Delta u_1 - \Delta T_e - D\Delta X_2) \quad (9)$$

$$\Delta X_3 = \frac{1}{T'_{d0}}(\Delta u_2 - \Delta X_3 - (X_d - X'_d)\Delta i_d) \quad (10)$$

$$\Delta i_d = \frac{\Delta X_3}{X'_d} + \frac{V_o \sin X_{10} \Delta X_2}{X'_d} = Y_d \Delta X_3 + F_d \Delta X_1 \quad (11)$$

$$\Delta T_e = (C_3 \sin X_{10})\Delta X_3 + (C_3 X_{30} \cos X_{10} + 2C_4 \cos 2X_{10})\Delta X_1 \quad (12)$$

Substituting (11) and (12) in (9) and (10) the following linear state equation is obtained.

$$\begin{bmatrix} \Delta\dot{X}_1 \\ \Delta\dot{X}_2 \\ \Delta\dot{X}_3 \end{bmatrix} = \begin{bmatrix} 0 & \omega_0 & 0 \\ \frac{-k_1}{M} & \frac{-D}{M} & \frac{-k_2}{M} \\ \frac{-k_4}{T'_{d0}} & 0 & \frac{-1}{k_3 T'_{d0}} \end{bmatrix} . \begin{bmatrix} \Delta X_1 \\ \Delta X_2 \\ \Delta X_3 \end{bmatrix} + \begin{bmatrix} 0 & 0 \\ \frac{1}{M} & 0 \\ 0 & \frac{1}{T'_{d0}} \end{bmatrix} . \begin{bmatrix} u_1 \\ u_2 \end{bmatrix} \quad (13)$$

Where

$$k_1 = C_3 X_{30} \cos X_{10} + 2C_4 \cos 2X_{10}$$

$$k_2 = C_3 \sin X_{10}$$

$$k_3 = \frac{1}{1 + (X_d - X'_d)Y_d}$$

$$k_4 = (X_d - X'_d)F_d$$

$$Y_d = \frac{1}{X'_d}$$

$$F_d = \frac{V_o \sin X_{10}}{X'_d}$$

T_m is mechanical input torque; T_e is electromagnetic torque of machine; M and D are inertia constant and damping coefficient of machine respectively; ω_0 is synchronous speed; E_{fd} is excitation voltage; X_d and X'_d are synchronous and transient d-axis machine reactance respectively; X_q is synchronous q-axis machine reactance; δ is power angle; T'_{d0} is open circuit time constant of the machine and X_{10} is the initial value of power angle.

III. ROBUST CONTROL

Using a suitable robust control, the closed-loop system remains stable even in the presence of system uncertainties. Most of these uncertainties are due the approximation in modeling the system. Usually in system modeling small time constants and some nonlinear and time varying terms are neglected. To retain the good performance of the closed-loop system despite these approximations, a robust controller is design for introduced power system [6].
Considering model uncertainties, the state equation

$$\dot{X}(t) = AX(t) + BU(t) \quad (14)$$

Is written as

$$\dot{X}(t) = (A + D\Delta(t)E_1)X(t) + (B + D\Delta(t)E_2)U(t) \quad (15)$$

Where $\Delta(t)$ represents an scalar or matrix including uncertainties which is satisfied $\Delta^T(t)\Delta(t) \le I$, D, E_1 and E_2 are scalars or matrices relating to uncertainties coefficients.
In control theory, the main aim is the obtaining of a stabilizing

Feedback gain (state feedback) as follow:

$$U = KX \quad (16)$$

To solve this control problem the following matrix inequalities are used:

$$\begin{bmatrix} G_1 & G_2^T & QR_1^{1/2} & Y^T R_2^{1/2} \\ G_2 & -\varepsilon I & 0 & 0 \\ R_1^{1/2} Q^T & 0 & -I & 0 \\ R_2^{1/2} Y & 0 & 0 & -I \end{bmatrix} < 0 \quad (17)$$

$$G_1 = QA^T + AQ + BY + Y^T B^T + DMD$$

$$G_2 = E_1 Q + E_2 Y$$

Where:

$$\varepsilon > 0 \quad (18)$$

$$Q > 0 \quad (19)$$

In these LMIs, Y is a variable without sign; R_1 and R_2 are positive definite constants relating to the following H_2 cost function:

$$J = \int_0^\infty (X^T R_1 X + U^T R_2 U) dt$$

Using MATLAB coding the following state feedback gain can be obtained:

$$K = YQ^{-1} \tag{20}$$

IV. TUNING BY PARTICLE SWARM OPTIMIZATION

Particle swarm optimization (PSO) was introduced in 1995 by Kennedy and Eberhart [7].

In PSO algorithm, a random population of points is generated. Each point represents a member of the population. In PSO algorithm there is no sudden jump or confusion; each point is a solution. Considering X and V as particle position and velocity respectively, the position of n^{th} particle in a space with m dime is represented with $X_n = [X_{n1}, X_{n2}, ..., X_{nm}]$.

The position of each particle is changed in next stage and it reaches a new position. The best position of n^{th} particle which is corresponding with the lowest cost function for that particle is saved in P_{best_n} .In addition, P_{best} of all particles are compared and the position of particle which has the lowest cost function is saved in G_{best} . The next vector of each particle is depending on its position and its distance to its P_{best} and its distance to G_{best} .The relations of particles movements are as follow:

$$V_{nm}^{i+1} = w \times V_{nm}^{i} + C_1 \times rand() \times (P_{best_{nm}} - X_{nm}^{i} + C_2 \times rand() \times (G_{best} - X_{nm}^{i})) \tag{21}$$

$$X_{nm}^{i+1} = X_{nm}^{i} + CV_{nm}^{i+1} \tag{22}$$

$$\left|V_{nm}^{i+1}\right| \le V_{\max} \tag{23}$$

Where $V_{\max}$ is a parameter that prevents to go out of suitable search space which causes the solution to be in acceptable region; C_1 and C_2 are constants which represent the speed of learning or pulling to P_{best} and G_{best} ; the weighing function w is given by:

$$w = w_{\max} - \frac{w_{\max} - w_{\min}}{iter_{\max}} \times iter \tag{24}$$

Here $w_{\min}$ and $w_{\max}$ are minimum and maximum of weighing function; $iter$ is the number of iterations.

In order to optimize the parameters of the controller with PSO, the following cost function is used

$$CostFunction = \int_0^{t_1} t_s \left|e(t)\right| dt \tag{25}$$

Where t_1 is the final time of simulation; e is the error signal and t_s is the settling time of the system.

V. SIMULATION AND RESULTS

To show the effectiveness of the proposed controller, simulation results are demonstrated in this section. The simulation results are obtained for two cases: without considering uncertainties and with considering uncertainties. Using the model and system parameters the following state space and control matrices are obtained,

$$A = \begin{bmatrix} 0 & 376.9911 & 0 \\ -0.0286 & 0 & -0.0748 \\ -0.1683 & 0 & -0.4371 \end{bmatrix}$$

$$B = \begin{bmatrix} 0 & 0 \\ 0.0893 & 0 \\ 0 & 0.1874 \end{bmatrix}$$

To obtain the coefficients and parameters of (15) two cases are considered.

A. *Without considering uncertainties*

In this case these coefficients and parameters are given by

$$E_1 = E_2 = 0$$

$$D = 0$$

The parameters of the proposed controller R_1 and R_2 should be positive definite. In first step, they selected as unitary matrices. Using these matrices, some machine input variables become out of reasonable range. With PSO algorithm the optimal matrices are obtained as

$$R_1 = \begin{bmatrix} 3.19 & 0 & 0 \\ 0 & 47.53 & 0 \\ 0 & 0 & 0.000001 \end{bmatrix}$$

$$R_2 = \begin{bmatrix} 58.81 & 0 \\ 0 & 142.1 \end{bmatrix}$$

With MATLAB coding the following state feedback gain is obtained

$$K = \begin{bmatrix} -0.0378 & -27.9272 & 0.165 \\ -0.0055 & 0.1430 & -0.0394 \end{bmatrix}$$

The obtained results for sudden change in load are represented as follow.

Assuming a 500MW load is omitted from the power grid at t=0.1sec and it is returned after t=1.1sec. This test illustrates the dynamic stability of the system clearly. The obtained results are shown in Figs. (2)-(4). As can be seen from these figures, again the oscillations are damped rapidly and the

maximum overshoot is small. The machine power angle has little oscillations. After the load variations, machine return to steady-state conditions.

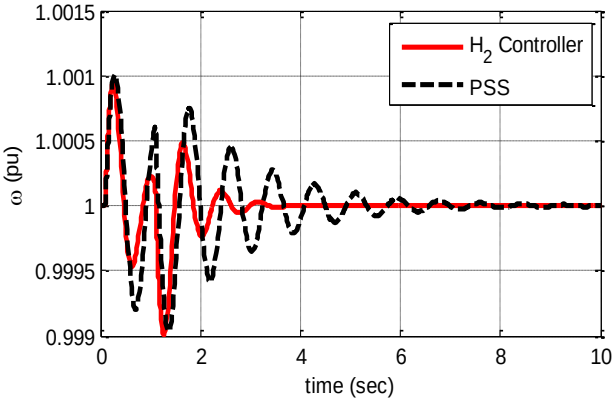

Fig. 2. Machine rotor speed for sudden variations of load

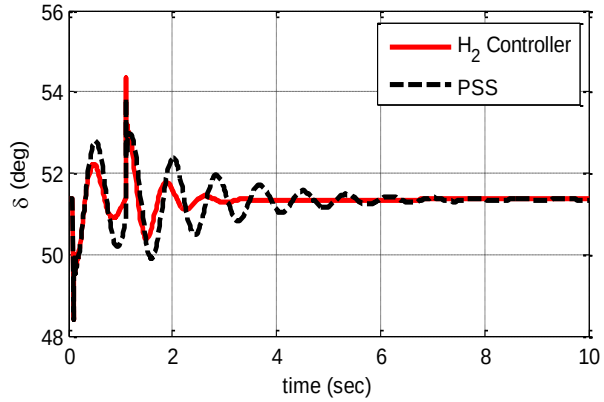

Fig. 3. Machine torque angle for sudden variations of load

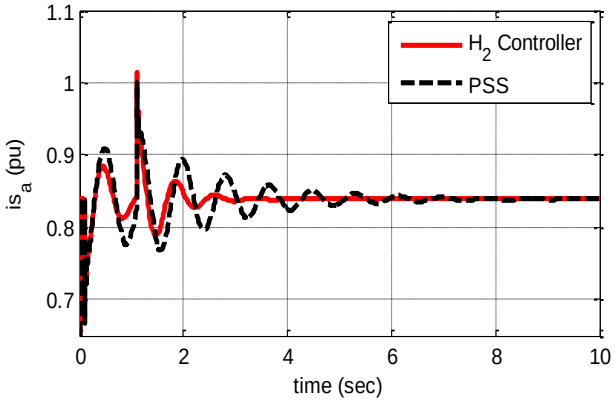

Fig. 4. Machine phase 'a' current for sudden variations of load

B. *Power system with parametric uncertainties*

In this section, it is assumed that there are uncertainties in damping coefficient (D) and inertia constant (H) of synchronous machine. The uncertainty in D is modeled as

$$\frac{D+\delta_D}{M}=\frac{D}{M}+\frac{\delta_D}{M} \tag{26}$$

Using the following geometric series

$$\frac{1}{1-a}=1+a+a^2+a^3+\ldots \tag{27}$$

The uncertainty in H is modeled as follow

$$\frac{-k_1}{2(H+\delta_H)}=\frac{-k_1}{2H(1+\frac{\delta_H}{H})}=\frac{-k_1}{2H}+\frac{k_1}{2H^2}\delta_H \tag{28}$$

In (28) and (30), δ_D and δ_H represent the uncertainties in D and H respectively.
The matrices of (17) is given by,

$$E_1=\begin{bmatrix}0 & \frac{-1}{2H} & 0\\ \frac{-k_1}{2H^2} & \frac{D}{2H} & \frac{-k_2}{2H^2}\end{bmatrix}$$

$$E_2=\begin{bmatrix}0 & 0\\ \frac{-1}{2H^2} & 0\end{bmatrix}$$

$$D=\begin{bmatrix}0 & 0\\ 1 & 1\\ 0 & 0\end{bmatrix}$$

The matrices R_1 and R_2 using PSO algorithm after 100 iterations are obtained as,

$$R_1=\begin{bmatrix}6.6907 & 0 & 0\\ 0 & 45.2011 & 0\\ 0 & 0 & 0.1026\end{bmatrix}$$

$$R_2=\begin{bmatrix}78.0133 & 0\\ 0 & 35.3664\end{bmatrix}$$

Using MATLAB software, the state feedback gain is obtained as,

$$K=\begin{bmatrix}-0.1549 & -57.0393 & 0.0819\\ -0.0781 & 1.0032 & -0.3686\end{bmatrix}$$

Assuming a 500MW load is omitted from the power grid at t=0.1sec and it is returned after t=1.1sec in the presence of uncertainties. The obtained results are shown in Figs. (5)-(7). As can be seen from these figures, again the oscillations are damped rapidly and the maximum overshoot is small. The machine power angle has little oscillations. Conventional PSS operates very weak in this test.

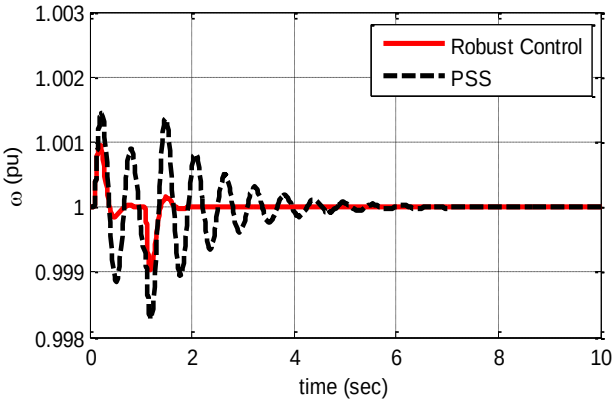

Fig. 5. Machine rotor speed for sudden variations of load

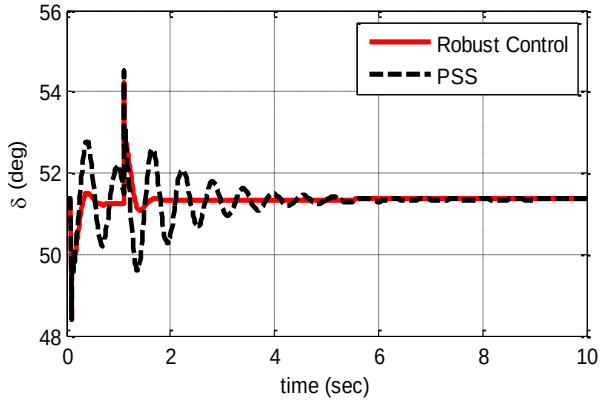

Fig. 6. Machine torque angle for sudden variations of load

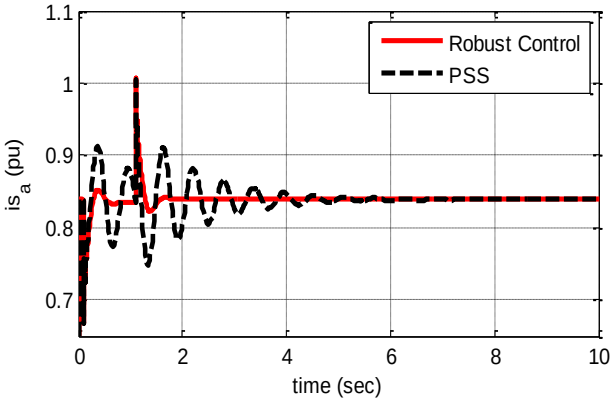

Fig. 7. Machine phase 'a' current for sudden variations of load

VI. Conclusion

Considering the capability of robust control in the presence of uncertainties, in this paper, a robust H_2 state feedback controller is designed for a power system. Parameters of the controller are tuned using PSO algorithm. The performance of the closed-loop system is investigated without and with uncertainties in the mechanical parameters with sudden load variation.

The obtained simulation results show the superiority of the proposed controller over conventional PSS. Using the proposed conventional the oscillations have a small amplitude and they are damped rapidly.

VII. Appendix

System data for single machine infinite bus power system Generator [8]:

$$H=5.6\ X_d=1.8pu\ X_q=1.8pu\ D=1pu\ X'_d=0.32pu$$
$$T'_{d0}=5.3371\text{sec}\ f=60Hz$$

Transmission Line and Load:

$$R=0.1273pu\ X=0.85pu\ G=0.27027pu$$
$$B=0$$

Exciter (simplified IEEE type-ST1):

$$K_A=10\ T_A=0.01\text{sec}$$

References

[1] Qihua Zhao; Jin Jiang, "*Robust SVC controller design for improving power system damping*,"*Power Systems, IEEE Transactions on* , vol.10, no.4, pp.1927,1932, Nov. 1995.

[2] Kanojia, S. S.; Chandrakar, V. K., "*Coordinated tuning of POD and PSS controllers with STATCOM in increasing the oscillation stability of single and multi-machine power system*,"*Engineering (NUiCONE), 2011 Nirma University International Conference on* , vol., no., pp.1,5, 8-10 Dec. 2011.

[3] Datta, S.; Roy, A.K., "*Fuzzy logic based STATCOM Controller for enhancement of power system dynamic stability*,"*Electrical and Computer Engineering (ICECE), 2010 International Conference on* , vol., no., pp.294,297, 18-20 Dec. 2010.

[4] Kannan Sreenivasachar, S. Jayaram, M.M.A. Salama, "*Dynamic stability improvement of multi-machine power system with UPFC*," Electric Power Systems Research, Volume 55, Issue 1, 5 July 2000.

[5] Wang, Z.; Chung, C.Y.; Wong, K.P.; Tse, C. T., "*Robust power system stabiliser design under multi-operating conditions using differential evolution*," *Generation, Transmission & Distribution, IET* , vol.2, no.5, pp.690,700, September 2008.

[6] S.Boyd, L.El Ghaoui, E.Ferdon and V.Balakrishnan, "*Linear Matrix Inequalities in System and Control Theroy*,"SIAM, 1994.

[7] J. Kennedy and R. C. Eberhart, "*Particle swarm optimization*," in *Proc. IEEE Int.Conf. Neural Networks* . Perth. Australia, pp, 1942-1948, 1995.

[8] P.C.Krause, "*Analysis of Electric Machinery*." New York: McGrawHill, 1986.

Biographies

M. Mohseni Mirabadi received the B.Sc. degree in electrical engineering from Khomeinishahr Branch, Islamic Azad University, Isfahan, Iran, in 2010 and the M.Sc. degree in electrical engineering from the Shahrekord University, Shahrekord, Iran, in 2013. His research interests are robust and nonlinear control, power system control and stability and linear matrix inequality.

N. R. Abjadi received the B.Sc., M.S., and Ph.D. degree all in electrical engineering from Isfahan University of Technology, Isfahan, Iran, in 1999, 2002, and 2010 respectively. He is currently an assistant professor in the electrical engineering in the faculty of engineering, Shahrekord University, Shahrekord, IRAN. His main research interests are application of nonlinear control and electric motor drives in general.

S. Hoghoughi-Isfahani received the B.Sc. degree from Sharif University of Technology, Tehran, Iran in 1989, the M.S. degree from Amir-Kabir University of Technology, Tehran, Iran, in 1993 and the Ph.D. degree from University of New South Wales, Canberra, Australia, in 1999. He is currently an assistant professor in the electrical engineering in the faculty of engineering, Shahrekord University, Shahrekord, Iran. His research interests are robust control, linear matrix inequality, and guaranteed cost function control.

S. Shojaeian received the B.Sc. and M.S. degree from Isfahan University of Technology, Isfahan, Iran, in 1997 and 2001 respectively and the Ph.D. from Islamic Azad University, science and research branch, Tehran, Iran in 2012. He is currently an assistant professor in the department of electrical engineering Khomeinishahr branch, Islamic Azad University, Isfahan, IRAN. His research interests are nonlinear control application in power system and power system stability and reliability.

Balkan Journal of Electrical & Computer Engineering
BAJECE
An International Peer Reviewed Refereed indexed and Open Access Journal

ISSN: 2147- 284X
Vol: 2
No: 1
Year: March 2014

CONTENTS

BALKAN JOURNAL OF ELECTRICAL & COMPUTER ENGINEERING

(An International Peer Reviewed, Refereed, indexed and Open Access Journal**)**

Contact
www.bajece.com
e-mail: editor@bajece.com
bajece@bajece.com

Phone: +90 288 214 05 14
Fax: +90 288 214 05 16

Kirklareli University,
Engineering Faculty,
Department of Electrical & Electronics Engineering,
39020, Kirklareli-Turkey.